NOTES ON NEUTRON DEPTH PROFILING

by

J.K. Shultis

Department of Mechanical and Nuclear Engineering
Kansas State University
Manhatta, Kansas 55606

published as

Report 298

Notes on Neutron Depth Profiling

J. Kenneth Shultis

December 2003

1 Introduction

The purpose of neutron depth profiling (NDP) is to determine the concentration (atoms/cm^3) of a particular isotope or element as a function of depth from the surface of a sample. In this technique, the sample, placed in a vacuum chamber, is irradiated by a beam of thermal neutrons. The concentration profile is then inferred from the energy distribution of ions that are produced by neutron interactions with the isotope of interest and that reach the sample's surface after losing some of their initial kinetic energy while traveling through the sample to the surface. The energies of ions escaping the sample surface is measured by an appropriate solid-state ion detector, also in the vacuum chamber, whose signal is fed to a multichannel analyzer (MCA). From the resulting MCA spectrum, the concentration profile of the isotope of interest can be inferred. Because the range of ions with a few MeV of kinetic energy, typical of those produced by neutron interactions, is only several μm in condensed matter, the NDP method can be used to determine the concentration profile within only the first several μm below the surface.

In this report, the basic theory of how the MCA spectrum is related to the desired concentration profile is presented for the special case that the sample has a plane surface, a portion of which is uniformly illuminated by thermal neutrons. Several models are outlined for estimating the expected MCA ion-energy spectrum. The inverse problem of how to determine the concentration profile from the MCA spectrum is considered and several examples are given.

2 NDP without Energy Broadening

We begin by first discussing the ideal case in which there is no energy broadening in the measured spectrum. In this case the detector has perfect energy resolution and ions that are born at the same depth and reach the detector all have the same energy. In a later section we consider the more realistic case in which there is a spread of energies detected by the spectrometer of ions produced at the same depth in the sample. Consider the ideal neutron depth profiling (NDP) arrangement shown in Fig. 1. In a vacuum chamber a thermal neutron beam of cross sectional area A_n and with a uniform thermal flux density ϕ_t illuminates the plane surface of a sample at an angle θ_n to the surface normal. Ions produced by neutron interactions in the sample, e.g., the α and Li ions from the ^{10}B(n,α)^{7}Li reaction, are produced with well-defined initial kinetic energies. Some of these charged ions, which are produced isotropically in the sample, travel through the sample material, reach the sample surface and, subsequently, stream a distance r_d through the vacuum to reach an ion detector. The detector is assumed to have a plane surface of area A_d whose normal is at an angle θ_d to the sample normal.

As an ion, produced at depth x, travels to the sample surface, it looses some of its initial kinetic energy through ion-electron and, in frequently, ion-nucleus interactions. The greater its path length in the sample before reaching the surface, the lower is its kinetic energy as it escapes the surface. In principle, the measured energy spectrum of ions reaching the sample surface can be used to estimate the rate at which ions are produced at different depths in the sample. Because the production rate of ions is proportional to the concentration of the isotope that interacts with the neutrons to produce the ions as reaction products. Thus, the energy distribution $N(E)$ of ions escaping the sample surface can be used to infer the concentration profile $C(x)$ in the sample of the interacting isotope. In this section, the ideal relation between $N(E)$ and $C(x)$ is derived.
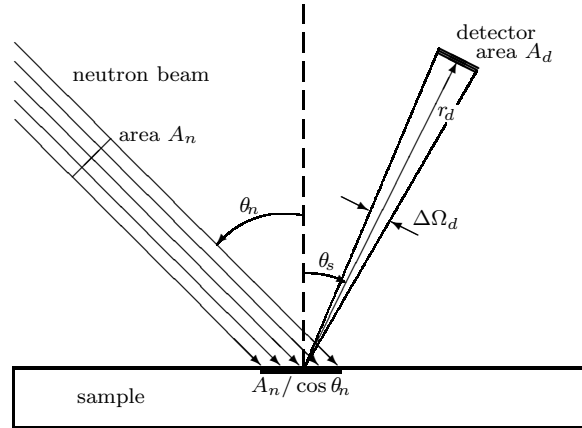
Figure 1. The basic NDP experimental arrangement.

2.1 Stopping Power and Residual Energy

Ions born with initial energy E_o travel through the sample material, ideally in straight lines,[1] loosing small amounts of energy from thousands of ion-election ionizing and excitation iterations per unit path length of travel. The rate at which energy is lost by the ion per unit path length of travel, $(-dE/dx)$, is called the ion *stopping power* $S(E)$ and typically has units of MeV/μm.

After travelling a distance s in the source material, the ion has a *residual energy* $E(s)$ given by

$$s = \int_0^s dx = \int_{E_o}^{E(s)} \left(\frac{dx}{dE'} \right) dE' = \int_{E_o}^{E(x)} \left(\frac{1}{-S(E')} \right) dE' = \int_{E(s)}^{E_o} \frac{dE'}{S(E')}. \tag{1}$$

If $E(s) \to 0$, $s \to \Lambda_o$, the *range* of the ion in the source material. This range defines the maximum depth into the sample for which NDP can be used.

2.1.1 Empirical Results for Stopping Power and Residual Energy

The analysis of ion energy spectra obtained using the neutron depth profiling (NDP) technique to obtain ^{10}B concentration profiles in silicon samples requires knowledge of how the alpha ^{4}He and ^{7}Li ions produced in the ^{10}B$(nm\alpha)^7$Li reaction interact in silicon. Specifically, one needs (1) the stopping power of the ions at all energies, (2) the residual energy of an ion after travelling a distance less than its range, (3) the path length required to reduce an ion from its initial energy any lower energy, and (4) the energy straggling (measured by the standard deviation of the ion energy) after travelling a specified distance in silicon.

The SRIM Monte Carlo code package [Ziegler and Biersack 2002] provides such ion interaction data. With this package, interaction data for helium and lithium ions in silicon was obtained, and empirical formulas were fitted to these data. The fitting was performed by TableCurve [Jandel 1998] which fits many thousands of different equations to given data and ranks the fits according the degree of agreement between the fit and data (here a χ^2 statistic). The selected fit was chosen by

---

[1]Large angle nuclear scattering interactions are rare but do occur. Also multiple small-angle scatters frequently occur resulting in energy broadening of the ions reaching the sample surface. These effects are not considered here but are discussed later in Section 3.

selecting the fit with relatively few free parameters and that had good agreement with the data, The results of these empirical fits are reported here.
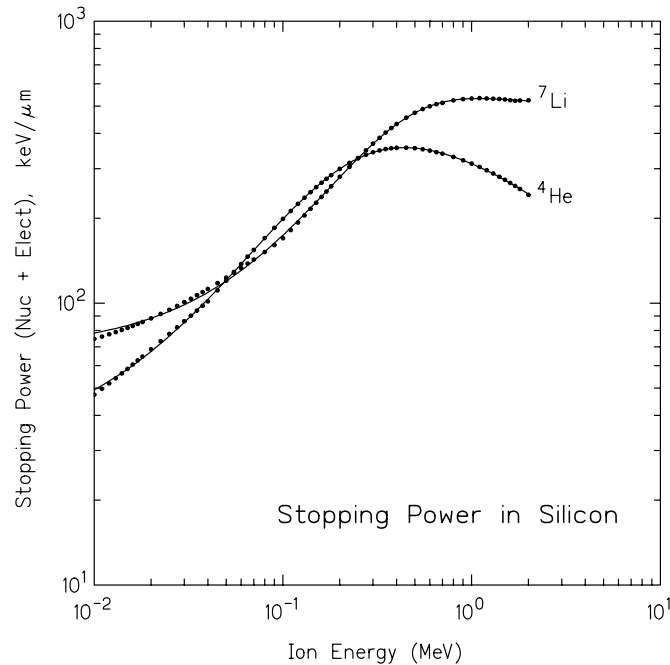
Stopping Power

An empirical formula for the stopping power in silicon is

$$S(E) \equiv \left(-\frac{dE}{ds} \right) = \frac{a + cE + eE^2}{1 + bE + dE^2 + fE^3} \qquad (2)$$

where $S(E)$ has units of keV/μm and E is the ion energy in MeV. Equation 2 is valid for $0.01 \leq E \leq 2$ MeV. Parameters for this fitting formula are given in Table 1 and a comparison of the fit to the TRIM data is shown in Fig. 2.

Table 1. Parameters of Eq. (2) for the empirical formula for the stopping power

Parameter in Eq. (2)	α particle	^{7}Li ion
a	31.061478	68.389815
b	1.8137558	-0.037458064
c	1862.3846	974.00508
d	14.803816	3.9534614
e	4772.0507	1454.8708
f	3.735421	-0.21760158

Figure 2. Stopping power $= dE/ds$ for helium and lithium-7 ions in silicon. Circles are data calculated by the TRIM code and lines are the empirical fits of Eq. (2).

3

Residual Energy

In principle, the residual energy $E(s)$ of an ion after travelling a distance s in a given material could be found by solving Eq. (1) for $E(e)$. However, as ions travel through a material some undergo multiple small angle scatters so that for the same geometric distance to the surface of a sample, ions will have slightly different path lengths and, thus, slightly different energies.

In our NDP analyses, we will need the *mean residual energy* $\overline{E}(x)$ of ions after they have travelled a geometric distance x in a given material. The mean residual energy was investigated using the Monte Carlo TRIM code of the SRIM package [Ziegler and Biersack 2002]. For a specified thickness x of silicon, the exit energies of normally incident alpha and lithium ions were recorded (see Fig. 10. Based on $N \geq 10,000$ histories, the mean residual energy was estimate as

$$\overline{E}(x) = \frac{1}{N} \sum_{i=1}^{N} E_i, \tag{3}$$

where E_i is the energy of the i=th transmitted ion. These estimates of the mean residual for different thickness were then fit to an empirical formula with TableCurve [Jandel 1996].

An empirical formula that gives the mean residual energy (MeV) of the four $^{10}B(n,\alpha)^7Li$ ions after they have traveled a distance x (μm) in silicon is

$$\overline{E}(x) = \frac{a + cx + ex^2}{1 + bx + dx^2 + fx^3}. \tag{4}$$

Parameters for this fitting formula are given in Table 2 and a comparison of the fit to the TRIM data is shown in Fig. 3.

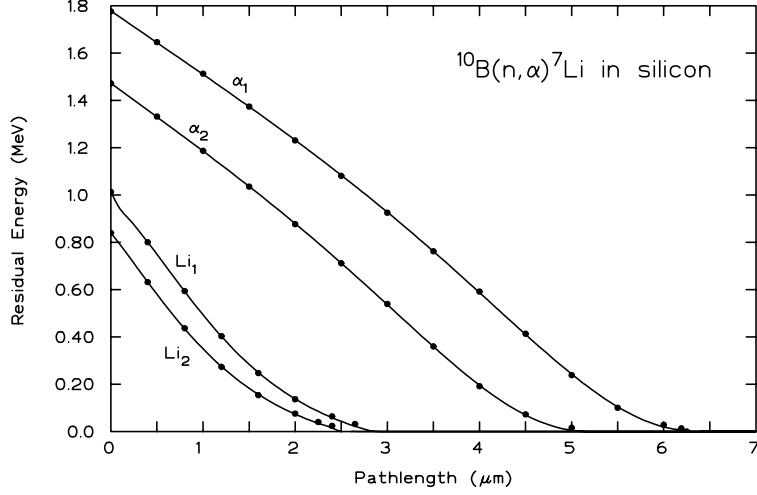**Table 2.** Parameters of Eq. (4) for the empirical formula for ion residual energy

Parameter in Eq. (4)	α_1	α_2	Li_1	Li_2
a	1.7785882	1.4731692	1.0132997	0.83979996
b	-0.16516657	-0.18960846	487.60039	7308.0497
c	-0.56309544	-0.56619005	476.75505	6150.5345
d	-0.0020145557	-0.0028652391	9.1891196	1456.6053
e	0.044594767	0.054390703	-168.03407	-2421.0822
f	0.0015759151	0.0032178631	129.50593	1899.8145

Path Length to Reach a Specified Residual Energy

An empirical formula that gives the path length x (μm) in silicon for $^{10}B(n,\alpha)^7Li$ ions to reach residual energy E (MeV) is

$$x(E) = a + bE + cE^{1.5} + dE^3 + c\exp(-E). \tag{5}$$

Parameters for this fitting formula are given in Table 3 and a comparison of the fit to the TRIM data is shown in Fig. 4.

Figure 3. Residual energy of an ion after travelling through silicon. Circles are data calculated by the TRIM code and lines are the empirical fits of Eq. (2).

Table 3. Parameters of Eq. (5) for the empirical formula for the path length needed to reach a given residual energy

| Parameter in Eq. (5)	α_1	α_2	Li$_1$	Li$_2$
a	52.018871	53.546724	16.994645	0.10642838
b	-59.738396	-62.762173	-24.033867	-6.1114722
c	28.198743	29.509255	13.40238	6.8549249
d	-0.87714178	-0.85902922	-1.1234069	-2.10642838
e	-45.762079	-48.443298	-14.176564	2.3973523

2.2   Ideal NDP Spectrum

We assume the trace isotope of interest, which interacts with a thermal neutron to produce a charged ion as a reaction product, has a concentration $C(x)$ which varies with depth x from the sample surface. Further, we assume the thermal neutron flux ϕ_t in the neutron beam is spatially uniform and negligibly attenuated as it passes through the sample. In the beam, the rate at which ions are produced per unit volume at depth x in the sample is

$$F_{ion}(x) = C(x)\, f_{ion}\overline{\sigma}_{ion}\, \phi_t, \tag{6}$$

where $\overline{\sigma}_{ion}$ is the microscopic thermal-averaged cross section for ion production and f_{ion} is the fractional yield for the ion of interest per ion production reaction. For a beam with a Maxwellian thermal-neutron energy spectrum characterized by temperature T, the thermal-averaged cross section is related to the 2200-m/s (0.0253 eV) cross section σ_{ion}^o by

$$\overline{\sigma}_{ion} = \frac{\sqrt{\pi}}{2}g_{ion}(T)\sqrt{\frac{T_o}{T}}\,\sigma_{ion}^o,$$

where $T_o = 293$ K and $g_{ion}(T)$ is the Wescott non-1/v factor for the ion-producing cross section and usually equals unity for the light elements suitable for NDP analysis.

5
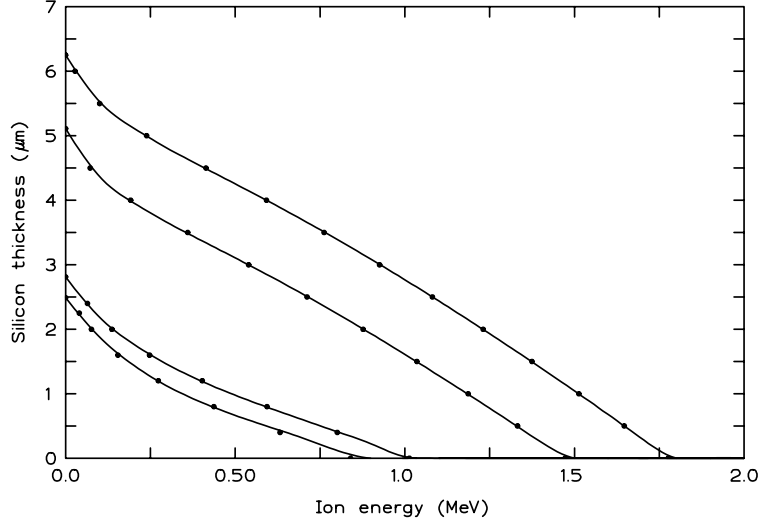
Figure 4. Path length in silicon versus the mean residual energy. Circles are data calculated by the TRIM code and lines are the empirical fits of Eq. (5).

The volume of irradiated sample material at depths within dx about x is $\Delta V = (A_n / \cos \theta_n) dx$, so that the number of ions produced per unit time at depths within dx about x is

$$N_{ion}(x)\, dx = F_{ion}(x)\, \Delta V = C(x)\, f_{ion}\overline{\sigma}_{ion}\, \phi_t \left(\frac{A_n}{\cos \theta_n} \right) dx. \tag{7}$$

We now assume the area of the sample surface illuminated by the neutron beam, $A_n / \cos \theta_n$ (see Fig. 1), is sufficiently small that all ion produced in the irradiated volume of the sample and reaching the detector are normally incident on the detector surface. Further, we assume the depth x at which the detector ions are produced is very small compared to the sample-to-detector distance r_d. This last assumption is almost always true since the maximum range of ions is typically several μm compared to r_d which typically is several cm. With these assumptions, the probability an ion, which is emitted isotropically from its point of birth, is

$$P_d = \frac{\Delta \Omega_d}{4\pi} = \frac{\Delta A_d}{4\pi r_d^2}, \tag{8}$$

where $\Delta \Omega_d$ is the solid angle subtended by the detector surface at the sample's irradiated surface. Finally, the detector efficiency per incident ion is denoted by ϵ and is the probability an incident ion produces a count in the in MCA spectrum. For most solid-state detectors $\epsilon \simeq 1$. With these assumptions, the number of ions detected per unit time that were produced within dx about x in the sample is

$$N(x)\, dx = [N_{ion}(x)\, dx][P_d][\epsilon] = C(x)\, f_{ion}\overline{\sigma}_{ion}\, \phi_t \left(\frac{\epsilon A_n}{\cos \theta_n} \frac{A_d}{4\pi r_d^2} \right) dx. \tag{9}$$

As seen from Fig. 5, the number of ions born in dx about x that reach the detector must travel through a distance $s = x / \cos \theta_s$ in the sample before reaching the surface and streaming to the detector. The energy of these escaping ions born at depth x, $E(x)$, is given by Eq. (1), i.e.,

$$s = \frac{x}{\cos \theta_s} = \int_{E(s)}^{E_o} \frac{dE'}{S(E')}. \tag{10}$$

6
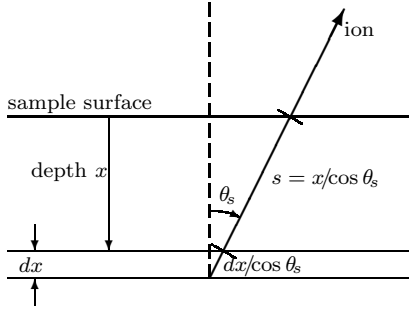
Figure 5. Path of ion born at depth x that reaches the NDP detector.

Let $N(E)\,dE$ be the number of ions with energies in dE about E that are measured by the detector per unit time. If E and x are related by Eq. (10), we must have

$$N(E)\,dE = -N(x)\,dx, \qquad (11)$$

where the minus sign is required since an increase in x results in a decrease of E. From Eq. (3) we find (from Leibnitz's rule for differentiation of an integral)

$$\frac{ds}{dE} = \frac{d(x/\cos\theta_s)}{dE} = -\frac{1}{S(E(s))}$$

or

$$\frac{dx}{dE} = -\frac{\cos\theta_s}{S(E(s))}, \qquad (12)$$

where $S(E(s))$ is given by Eq. (1) (or, better for numerical purposes, by an appropriate fit of s versus $E(s)$). Combining Eq. (11) and Eq. (12) one obtains the energy distribution of ions recorded by the detector, per unit time, namely

$$N(E) = N(x)\left(-\frac{dx}{dE}\right) = C(x)\,f_{ion}\overline{\sigma}_{ion}\,\phi_t\left(\frac{\epsilon A_n}{\cos\theta_n}\frac{A_d}{4\pi r_d^2}\right)\frac{\cos\theta_s}{S(E)}. \qquad (13)$$

or more compactly

$$\boxed{N(E) = \kappa\,\frac{C(x(E))}{S(E)},} \qquad (14)$$

where

$$\kappa \equiv f_{ion}\overline{\sigma}_{ion}\,\phi_t\left(\frac{\epsilon A_n}{\cos\theta_n}\frac{A_d\cos\theta_s}{4\pi r_d^2}\right). \qquad (15)$$

Here $x(E)$ is the depth for which the residual energy of the ion after travelling a distance $s = x/\cos\theta_d$ in the sample to reach the surface is E. This depth is given by Eq. (3) which can be rewritten as

$$x(E) = \cos\theta_s\int_E^{E_o}\frac{dE'}{S(E')}. \qquad (16)$$

Once the energy spectrum $N(E)$ of the ions is known or measured, the concentration profile is obtained directly from Eq. (14) as

$$\boxed{C(x) = \frac{1}{\kappa}\,N(E(s))\,S(E(s)),} \qquad (17)$$

where the residual energy $E(s)$ for ions born at depth x and that travel a distance s in the sample material is given by Eq. (3).

2.3 The MCA Ion-Energy Spectrum with No Energy Broadening

In this ideal case, the concentration profile is immediately given by Eq. (17) provided $N(E)$ is known. However, this later quantity must be estimated from the MCA channel counts y_i. The number of counts in channel i (midpoint energy E_i and width 2Δ) for a measurement time Δt are

$$y_i = \Delta t\int_{E_i-\Delta}^{E_i+\Delta}N(E)\,dE. \qquad (18)$$

7

This result can also be written in terms of the concentration profile $C(x)$ by substituting Eq. (13) into Eq. (18). The result

$$y_i = \Delta t \int_{E_i-\Delta}^{E_i+\Delta} N(E)\, dE = \kappa \Delta t \int_{E_i-\Delta}^{E_i+\Delta} \frac{C(x(E))}{S(E(s))}\, dE$$

$$= \kappa \Delta t \int_{x(E_i-\Delta)}^{x(E_i+\Delta)} \frac{C(x)}{S(E(s))} \left(\frac{dE}{dx}\right) dx = \kappa \Delta t \int_{x(E_i-\Delta)}^{x(E_i+\Delta)} \frac{C(x)}{S(E(s))} \left(-\frac{S(E(s))}{\cos\theta_d}\right) dx$$

$$= \frac{\kappa \Delta t}{\cos\theta_d} \int_{x(E_i+\Delta)}^{x(E_i-\Delta)} C(x)\, dx. \tag{19}$$

This last result can readily be written in the following general convolution form, whose inversion is considered later in Section 4,

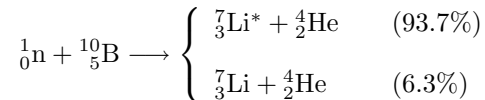$$\boxed{y_i = \int_0^{x_{\max}} C(x) R_i(x)\, dx.} \tag{20}$$

where the *channel response function* is

$$R_i(x) = \begin{cases} \dfrac{\kappa \Delta t}{\cos\theta_d}, & x(E_i+\Delta) < x < x(E_i-\Delta), \\[2mm] 0, & \text{otherwise.} \end{cases} \tag{21}$$

Here $x(E)$ is the depth from which the residual ion energy at the sample surface is E after traveling a path length $s = x/\cos\theta_s$. An empirical formula for this quantity is given by Eq. (5).

2.4   An Example Spectrum

The isotope ^{10}B is readily detected by NDP because of its large thermal-neutron cross section (3840 b at 0.00253 eV) for the ^{10}B(n,α)^{7}Li reaction. Two distinct energies of α and ^{7}Li ions are produced since the ^{7}Li nucleus is produced either in the ground state or in a 0.4776-MeV excited state as shown below.

$$^1_0 n + {}^{10}_5 B \longrightarrow \begin{cases} {}^7_3 \text{Li}^* + {}^4_2 \text{He} & (93.7\%) \\[2mm] {}^7_3 \text{Li} + {}^4_2 \text{He} & (6.3\%) \end{cases}$$

Alpha particles are produced with the two energies 1.7762 MeV (α_1) and 1.4721 MeV (α_2). The corresponding lithium ions have energies 1.0133 MeV (Li$_1$) and 0.8398 MeV (Li$_2$).

The National Institute of Standards and Technology (NIST) has prepared a reference NDP sample by implanting ^{10}B ions into a silicon substrate. This sample, known as SRM-2137, has a accurately measured ^{10}B concentration profile, which is shown in Fig. 6.

NDP spectra calculated by Eq. (14) generally will exhibit peaks that are narrower than in spectra obtained experimentally. This is to be expected, since the result of Eq. (14) is based on the assumption that all ions emitted at the same depth are recorded as having the same energy. In reality, slightly different energies are recorded as a result of several non-idealizations. The treatment of such *energy broadening* is the subject of the next section.
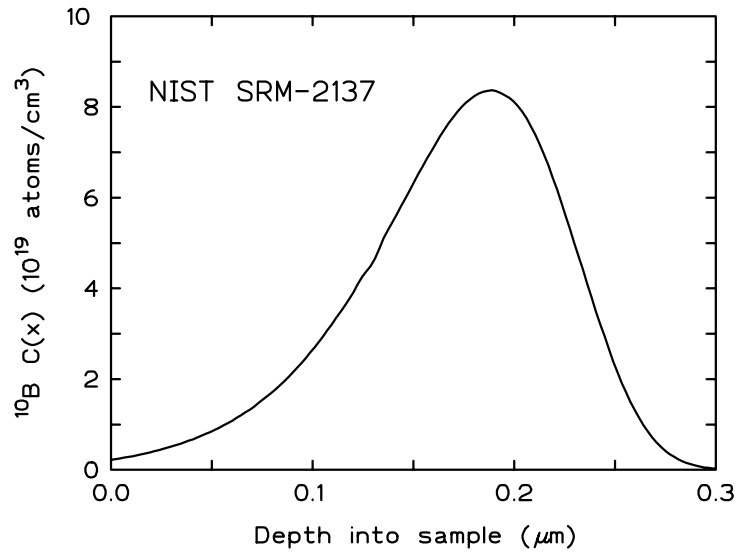
Figure 6. The ^{10}B concentration profile for the NIST SRM-2137 reference silicon waiver.
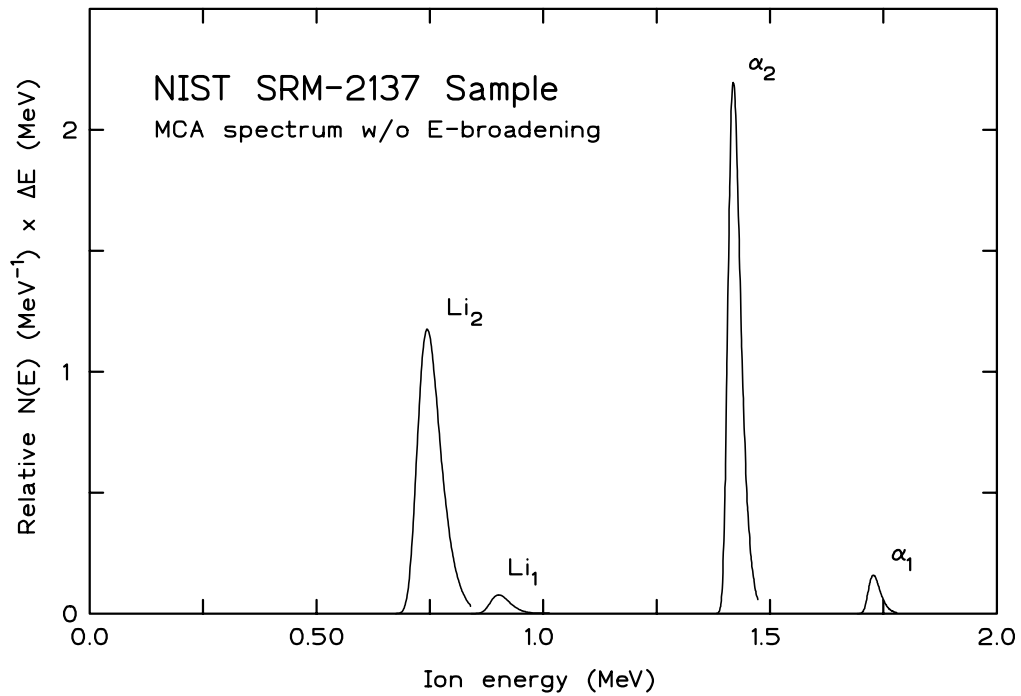
Figure 7. The ideal ion energy distribution as calculated by Eq. (14) without any energy broadening for the ^{10}B distribution shown in Fig. 6.

2.5 Inversion of the MCA Spectrum

The inversion of Eq. (21) to obtain $C(x)$ can be performed using the techniques discussed in Section 4. However, if the energy grid on the MCA spectrum is sufficiently fine such that $N(E)$ varies only slightly over a channel width, a much simpler approach can be used. For this special case of a fine energy mesh, Eq. (18) can be approximated as

$$y_i = \Delta t \int_{E_i - \Delta}^{E_i + \Delta} N(E) \, dE \simeq 2\Delta N(E_i) \Delta t, \tag{22}$$

from which we have $N(E_i) \simeq y_i / (2\Delta \, \Delta t)$. Then from Eq. (17) we immediate obtain

$$\boxed{C(x_i) \equiv C(x(E_i)) = \frac{y_i}{\Delta t} \frac{S(E_i)}{2\Delta \, \kappa}.} \tag{23}$$

An example of the estimated α_2 ion peak in the MCA spectrum for the NIST SRM-2137 is shown in Fig. 8. This spectrum was obtained from numerical evaluation of Eq. (20) using the certified ^{10}B concentration profile shown in Fig. 6. In inverted profile shown in Fig. 9 was obtained from Eq. (23).

3 NDP with Energy Broadening

In the ideal model of the previous section, the number of ions that escape the sample surface and are measured by the detector and that have a *mean* residual energy $dE(s)$ about $\overline{E}(s)$ is from Eqs. (11) and (13)

$$N(\overline{E}(s)) \, dE(s) = - \left[f_{ion} \overline{\sigma}_{ion} \, \phi_t \left(\frac{\epsilon A_n}{\cos \theta_n} \frac{A_d}{4\pi r_d^2} \right) \right] C(x) \, dx \equiv -\widehat{\kappa} C(x) \, dx, \tag{24}$$

where $\widehat{\kappa} \equiv \kappa / \cos \theta_s$, the constant in the square brackets.

The recorded energy of these ions will have a spread of energies about the mean residual energy as a result of (1) *energy straggling* as the ions travel through the sample material, (2) *detector energy broadening* caused by noise and the stochastic nature of ion reactions in the detector material, and (3) *geometric broadening* arising from the finite size of the detector and sample.

As ions travel through the sample material they undergo a myriad of stochastic interactions with the ambient atoms losing slightly different amounts of energy even though they travel exactly the same distance before reaching the surface. In addition, there are numerous small angle scatters that cause ions to travel slightly different distances in the sample before reaching the surface and, thereby, having a spread of energies. These two effects on the energy spreading are collectively referred to in this report as energy straggling.

The detector system itself broadens the measured ion energies as a result of its inherent resolution. Three contributions can be identified: (1) electronic noise of the amplifier chain, (2) intrinsic noise in the detector caused primarily by leakage currents, and (3) the stochastic variation in energy deposition by the ionizing interactions and stochastic competition with phonon production in the detector material.

Although the detector and irradiated area of the sample are generally small, they, nevertheless, have finite sizes. Ions leaving the sample at slightly different angles and exit points can still reach the detector. Thus, ions reaching the detector will have a distribution of path lengths in the sample and, consequently, a distribution of energies when they leave the sample. This effect is referred to as geometric broadening.
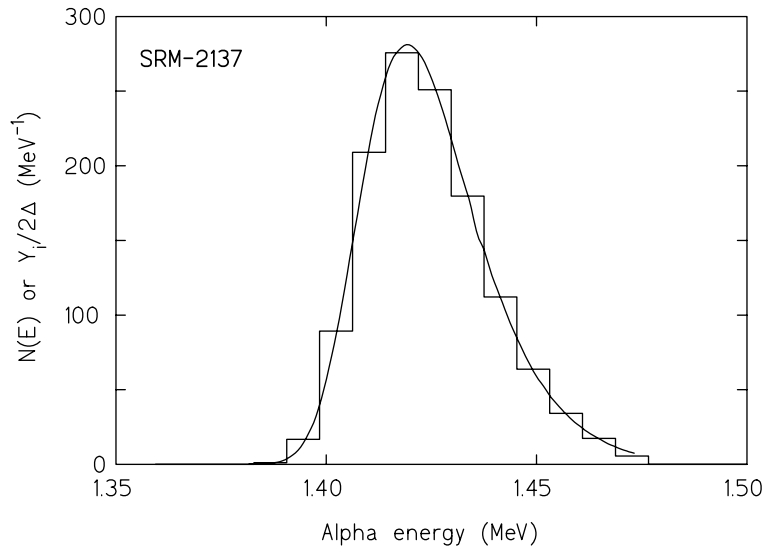
Figure 8. The ideal spectrum $N(E)$ and the predicted MCA spectrum for the 1.4721-MeV α particle of the ^{10}B(n,α)^{7}Li reaction in the NIST SRM-2137 silicon sample. The MCA spectrum was calculated from $N(E)$ by numerically evaluating Eq. (18).
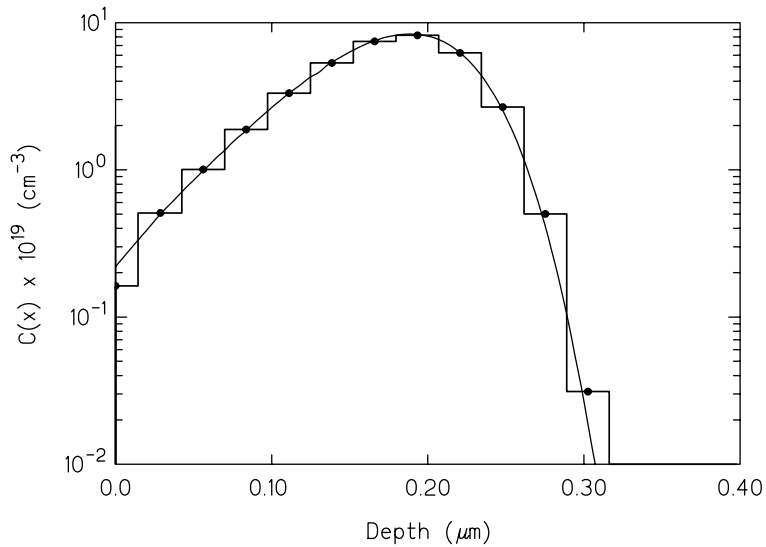
Figure 9. The actual and unfolded concentration profile $C(x)$ for the NIST SRM-2137 sample. The unfolded results were obtained using Eq. 23 and the predicted MCA spectrum shown in Fig. 8.

3.1 Spectral Broadening from Energy Straggling

The broadening of ion energies caused by energy straggling was investigated using the Monte Carlo TRIM code of the SRIM package [Ziegler and Biersack 2002]. For a specified thickness x of silicon, the exit energies of normally incident alpha and lithium ions were recorded (see Fig. 10. Based on $N \geq 10,000$ histories, the standard deviation of transmitted particle energies was computed as

$$\sigma_{strag}^2 = \frac{1}{N-1} \sum_{i=1}^{N} (E_i - \overline{E})^2, \tag{25}$$

where E_i is the energy of the ith transmitted ion and the mean transmitted (residual) energy is $\overline{E} = (1/N) \sum_{i=1}^{N} E_i$.

TRIM calculations of the energy straggling for the four ions produced in the ^{10}B(n,α)^{7}Li reaction were made and the following empirical equation was fit to the calculated results.

$$\frac{\sigma_{strag}}{E} = a + bE^c. \tag{26}$$

The empirical fit and the calculated energy straggling values are shown in Fig. 11. Values of the fitting parameters are given in Table 4.

Table 4. The initial energies, range in silicon, and the fit parameters for Eq. (26) for the ions produced in the ^{10}B(n,α)^{7}Li reaction.

| ion	E_o (MeV)	Range (μm)	Parameters for Eq. (26) a	b	c
α_1	1.7762	6.25	$-.087053189$	0.107157820	-0.37284172
α_2	1.4721	5.11	$-.084451428$	0.098519784	-0.37706387
Li$_1$	1.0133	2.81	$-.035292668$	0.043321774	-0.59331028
Li$_2$	0.8398	2.49	$-.049446492$	0.048381691	-0.56563867

3.2 Detector Energy Broadening

The recorded energy by the MCA is directly proportional to the amplitude of the pulse received by the MCA. Thus, any phenomenon that stochastically (or deterministically) varies the pulse amplitude will cause an apparent broadening of the recorded energies. For the NDP detector system there are two energy-broadening effects (1) system noise (σ_{noise}) and (2) stochastic variation of the amount of ionization produced by an ion in the detector crystal (σ_{ion}). The overall variance of the detector energy broadening is thus

$$\sigma_{det}^2 = \sigma_{noise}^2 + \sigma_{ion}^2. \tag{27}$$

The presence of noise in the detector and the amplifier chain perturbs the pulse amplitudes produced by the detector crystal, thereby, leading to a broadening of the recorded energy spectrum. The amount of the energy broadening is usually the same for all ion energies, i.e., $\sigma_{noise} \simeq$ constant.

On the other hand, the stochastic competition between phonon production and ionization by ions in the detector crystal produces different numbers of ionizing events for incident ions of the same initial energy. Because the detector pulse amplitude is directly proportional to the number of ionization event cause by the incident ion, the detector produces different pulse amplitudes leading to

12
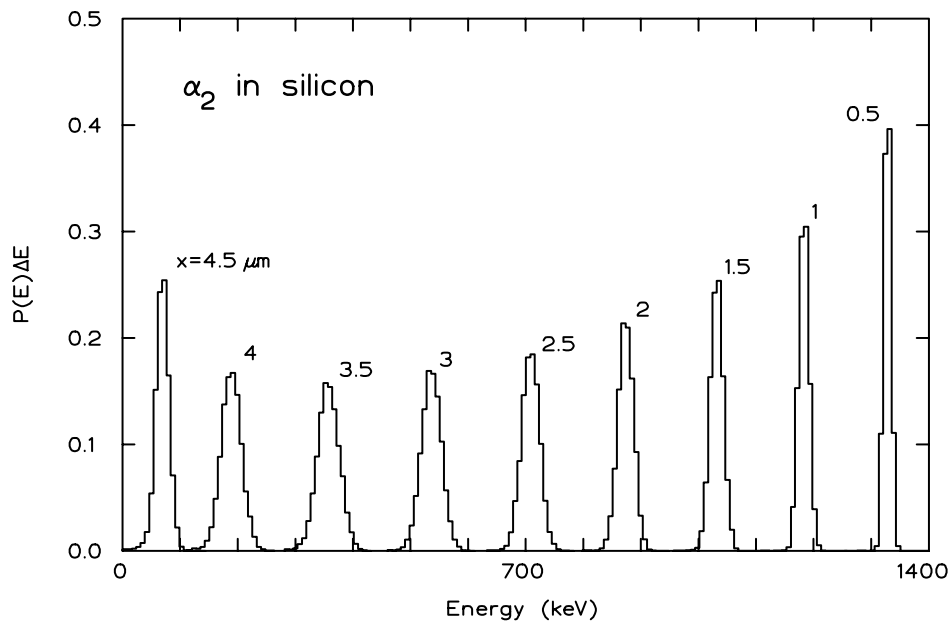
Figure 10. The distribution of energies of the α_2 ion from the $^{10}\mathrm{B}(\mathrm{n},\alpha)^{7}\mathrm{Li}$ reaction after traveling various distances in silicon. Each probability distribution was obtained using 10,000 histories from the TRIM simulation.
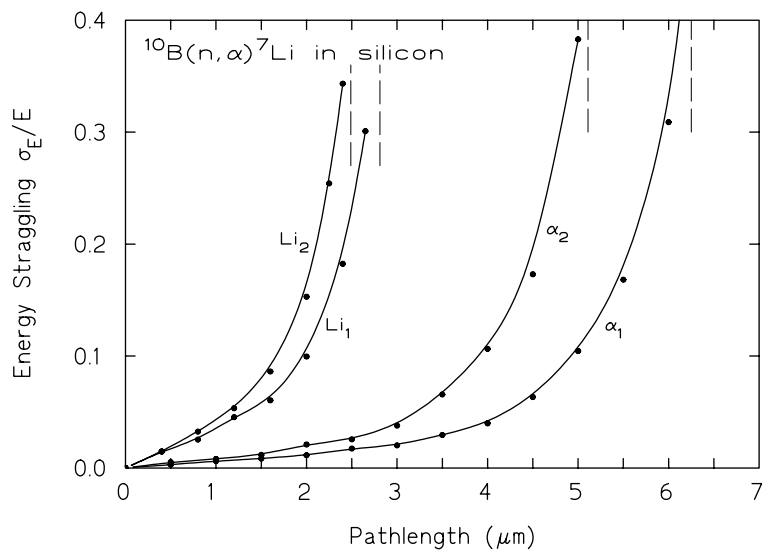
Figure 11. TRIM results for σ_{str}/E (circles) and the empirical fit of Eq. (25) (lines). The vertical dashed lines indicate the range in a silicon of each ion.

13

an apparent spread of ion energies. The magnitude of the spread, or variance σ_{ion}^2, of this stochastic ionization effect depends on the energy and charge of the ion as well as the detector material. For most solid state detectors there is negligible phonon production produced by ions of the hydrogen isotopes, and hence $\sigma_{ion} \simeq$ constant [Maki et al. 1986]. For ions with a charge greater than one, σ_{ion} generally cannot be neglected and is usually a function of the incident ion energy.

To determine the total detector system's energy broadening, $\sigma_{det}^2 = \sigma_{noise}^2 + \sigma_{ion}^2$, one generally must measure it by recording the MCA spectrum of monoenergetic ions of different energies (produced, say, by NDP measurements of a sample with a thin surface deposit of an ion producing isotope). In Fig. 12 we show a typical alpha peak produced by a sample with a surface coating of boron. Also shown are various Gaussian distribution fits to the data.
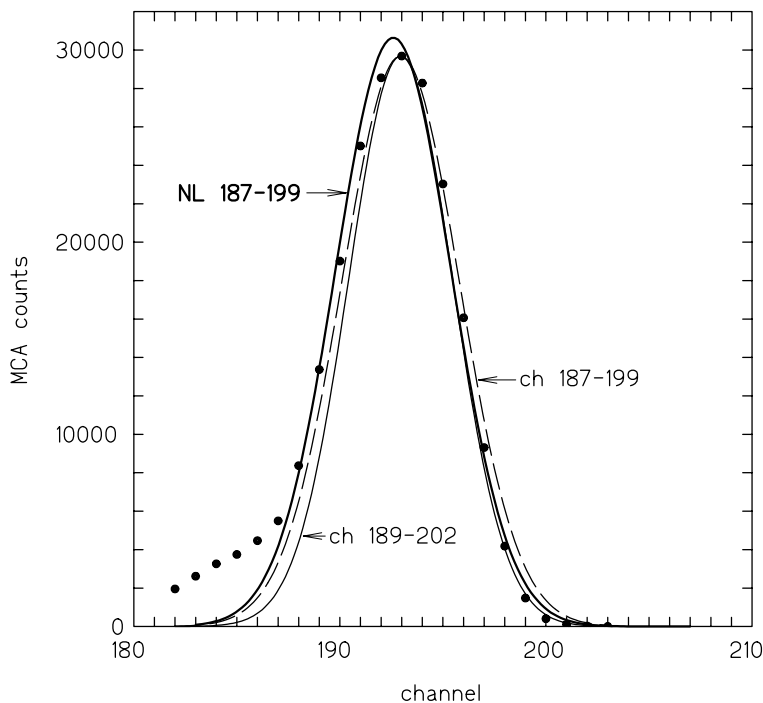
Figure 12. The geometric energy broadening for the 1.47-MeV α_2 ions produced in the ^{10}B(n,α)^{7}Li reaction. The circles are measured data and the lines are Gaussian distribution fits to the data using different methods and number of data.

3.2.1 Fitting a Gaussian Distribution to MCA Data

To determine the MCA system energy broadening variance σ_{det} it is necessary to fit a Gaussian distribution

$$y(E) = A \exp\left[-\frac{(E - E_p)^2}{2\sigma^2}\right] \tag{28}$$

to the MCA peak produced by an incident monoenergetic ion. Here the MCA data are the channel counts $y_n \equiv y(E_n), n = 1, ..., N$. Thus, we seek the Gaussian parameters A, E_p, and σ which gives the "best" agreement between the Gaussian distribution. Two methods are proposed.

Linear Transformation.   In this method, the first step is to estimate the peak amplitude A and its location E_p. A simple way is to fit a quadratic equation $y(E) = a + bE + cE^2$ to the peak channel count and the two bracketing channel counts $\{y_{m-1}, y_m, y_{m+1}\}$. The location of the maximum of

14

$y(E)$ is then $E_{\max} = -b/(2c) \simeq E_p$ and the peak value is $y(E_{\max}) = a + bE_{\max} + cE_{\max}^2 \simeq A$. Other more sophisticated method for estimating E_p and A can be used, but seldom seem worth the effort.

With estimated values for E_p and A, the standard deviation can be found by taking the logarithm of Eq. (28) and manipulating the result to obtain

$$G(E) \equiv \pm\sqrt{2\ln\left(\frac{A}{y(E)}\right)} = \frac{E}{\sigma} - \frac{E_p}{\sigma}. \tag{29}$$

The $+(-)$ sign in this result is used when $E > E_p$ ($E < E_p$). Plotting $G(E)$ versus E (or equivalently, plotting $G(E_n)$ versus n) yields a straight line whose slope is $1/\sigma$. The light lines in Fig. 12 were obtained in this manner.

Nonlinear Least Squares Fit. The above technique is rather *ad hoc*. A more rigorous approach is to perform a nonlinear fit by finding the values of A, E_p and σ than minimize the chi-squared statistic

$$\chi^2 = \sum_{n=1}^{N}\left[\frac{y_n - y(E_n)}{\sigma_n}\right]^2, \tag{30}$$

where $y(E)$ is given by Eq. (28) and $\sigma_n \simeq \sqrt{y_n}$ is the standard deviation of the count in channel n. This nonlinear minimization problem is readily perform numerically by using the `mrqmin` algorithm given by Press et al. [1992]. In Fig. 12 the heavy line shows the result of using a nonlinear least squares fit to the MCA data.

3.3   Spectral Broadening from Geometry Effects

Because of the finite sizes of the irradiated area of the sample and the detector, ions born at the same depth in the sample can travel in different directions and still reach the detector (see Fig. 13). The detected ions will therefore have slightly different residual energies as a result of having traveled different distances in the sample. This is the origin of geometric energy broadening.

We consider two cases. The first assumes the plane of the detector and the sample are parallel. Then a general formulation is presented in which the detector and sample planes can have arbitrary orientations.

### 3.3.1   Case of Parallel Sample and Detector Planes

To quantify the geometry effect for this particular geometry, consider a sample with an irradiated surface area A_s and a parallel detector plane of area A_d separated by a perpendicular distance h. As shown in Fig. 14, ions born at depth t in a differential area dA_s of the sample can reach a differential area dA_d of the detector by traveling along a ray at angle θ to the surface normal. The probability an ion born isotropically at dA_s will hit the detector element dA_d is the fraction of 4π steradians that the solid angle $d\Omega$ subtended by dA_d at dA_s, namely $d\Omega/4\pi = (dA_d \cos\theta_s)/4\pi r^2)$. The number of ions born at dA_s and that reach dA_d per unit time is thus

$$dN = \nu\, dA_s\left(\frac{dA_d \cos\theta_s}{4\pi r^2}\right), \tag{31}$$

where ν is rate of ion emission per unit area at depth t. These ions reaching dA_d all have a residual energy $E(s)$ where the sample path length is $s = t/\cos\theta_s$. The energy spectrum (number per unit energy) of these detected ions is then

$$dN(t, E) = \nu\left(\frac{\cos\theta_s}{4\pi r^2}\right) dA_s\, dA_d\, \delta(E - E(s)), \tag{32}$$

15
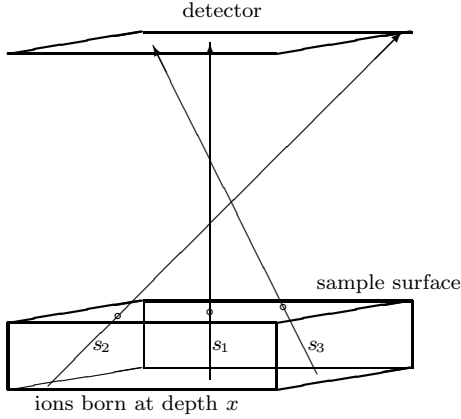
Figure 13. Geometric energy broadening occurs when ions born at the same depth can have different path lengths an still reach the detector.
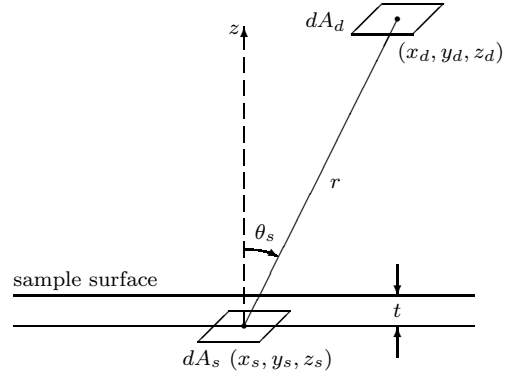
Figure 14. Geometry for estimating the geometry energy broadening effect. Ions born in dA_s travel a distance $s = t/\cos\theta_s$ to reach a differential area dA_d of the detector.

where $\delta(E - E(s))$ is the Kronecker delta function indicating that these ions are monoenergetic. If we select the outward normal to the sample surface as the z-axis, and if (x_s, y_s, z_s) and (x_d, y_d, z_d) are the coordinates of dA_s and dA_d, respectively, then in Eq. (32) we have

$$r^2 = (x_d - x_s)^2 + (y_d - y_s)^2 + (z_s - z_d)^2$$

$$\cos\theta_s = (z_d - z_s)/r \simeq h/r$$

$$s = t/\cos\theta_s \simeq t\,r/h.$$

Finally, the energy spectrum of all ions born at depth t across the irradiated area A_s and that reach the detector of area A_d is obtained by integrating Eq. (32) over all dA_s and dA_d, namely

$$N(t, E) = \nu \int_{A_s} dA_s \int_{A_d} dA_d \, \frac{\cos\theta_s}{4\pi r^2} \, \delta(E - E(s)). \tag{33}$$

This equation can be evaluated numerically by subdividing A_s and A_d into a set of small ΔA_{si} and ΔA_{dj} and replacing the integrals by the appropriate finite summations. An example result showing the geometric energy broadening is shown in Fig. 15. Notice that the energy broadening is a monotonic increasing distribution from the smallest energy (produced by the longest ion path) to the highest energy (produced by ions traveling the shortest perpendicular distance). For this example, it is seen that geometric energy broadening is relatively small compared to energy straggling and detector resolution effects.

From Eq. (33) we can obtain the moments of the energy distribution as

$$\mathcal{E}_n \equiv \langle E^n \rangle \equiv \int E^n N(t, E)\, dE \left/ \int N(t, E)\, dE \right. . \tag{34}$$

Substitution of Eq. (33) into this definition gives

$$\mathcal{E}_n = \int_{A_s} dA_s \int_{A_d} dA_d \, E^n(s) \frac{\cos\theta_s}{r^2} \left/ \int_{A_s} dA_s \int_{A_d} dA_d \, \frac{\cos\theta_s}{r^2} \right. . \tag{35}$$

16
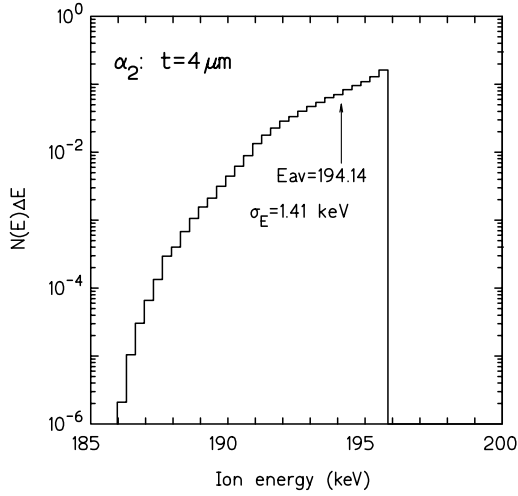
Figure 15. The geometric energy broadening for α_2 ions produced in the ^{10}B(n,α)^{7}Li reaction at a depth of 4 μm in silicon. Here the silicon sample and detector are 1-cm squares separated by 10.8 cm.
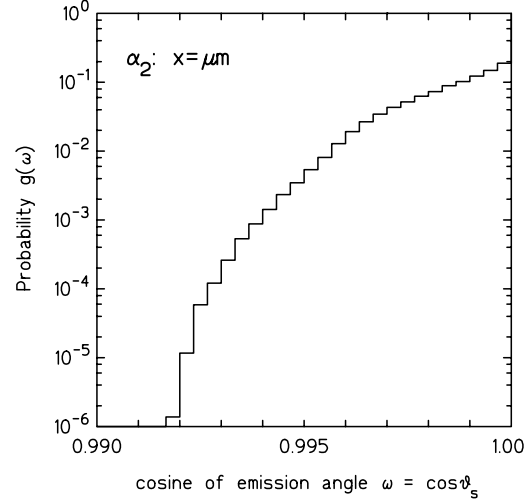
Figure 16. The probability the α_2 ions produced in the ^{10}B(n,α)^{7}Li reaction reaches the detector in unit cosine about the direction $\omega = \cos\theta$. Here the silicon sample and detector are 1-cm squares separated by 10.8 cm.

The average energy of an ion reaching the detector from a depth t in the sample is then

$$E_{av} = \langle E \rangle = \mathcal{E}_1, \tag{36}$$

and the variance in the energies is

$$\sigma^2_{geom} = \langle (E - E_{av})^2 \rangle = \mathcal{E}_2 - \mathcal{E}_1^2. \tag{37}$$

3.3.2 Emission Distribution for Parallel Samples and Detectors

The energy broadening produced by the geometry effect (e.g., Fig. 15) is generally poorly described by a Gaussian model and thus cannot be combined with other energy broadening effects into a single Gaussian distribution. Thus, geometric effects must be treated separately in describing the MCA ion-energy spectrum. This would appear to be an exceedingly difficult task, since from Eq. (33), $N(t, E)$ would have to be computed for an infinity of depths t at which ions are emitted in the sample.

However, an important observation can greatly simplify treating the geometry effect. The distribution $g(\theta)$ of ion directions that reach the detector, as measured by θ or $\omega \equiv \cos\theta$, is *independent* of t because t is negligible (micrometers) compared to the sample-detector separation (centimeters) [Cloakley et al. 1995]. The residual energy of an ion born at depth t and traveling to the detector at an angle θ_s is readily computed as $\overline{E}(s) = \overline{E}(t/\omega)$.

With the same argument used to obtained Eq. (32), the number of ions born in dA_s that reach dA_d within unit cosine about $\omega \equiv \cos\theta$ is

$$dN(t, \omega) \simeq dN(\omega) = \nu \left(\frac{\omega}{4\pi r^2} \right) dA_s \, dA_d \, \delta(\omega - \omega_s(\mathbf{r}_s, \mathbf{r}_d)), \tag{38}$$

where $\omega(\mathbf{r}_s, \mathbf{r}_d)$ is the cosine of the angle between the surface normals and the line joining dA_s (at location $\mathbf{r}_s$) and dA_d (at location $\mathbf{r}_d$). The number of ions reaching the detector from the sample in

unit cosine about the direction ω is then obtained by integrating the result over all dA_s and dA_d, namely

$$N(\omega) = \nu \int_{A_s} dA_s \int_{A_d} dA_d \frac{\omega}{4\pi r^2} \delta(\omega - \omega_s(\mathbf{r}_s, \mathbf{r}_d)). \tag{39}$$

This result can be readily evaluated numerically by subdividing A_s and A_d into sets of contiguous pixels of size ΔA_s and ΔA_d and replacing the integrals by appropriate summations.

Finally, the probability an ion born at *any* depth (with path length less than the ion's range) reaches the detector within unit cosine about the direction ω is computed as

$$g(\omega) = \frac{N(\omega)}{\nu A_s} \tag{40}$$

where νA_s is the total number of ions born at depth t. Usually, The detector and sample areas are small compared to the sample-detector distance, and, consequently, $N(\omega)$ and $g(\omega)$ are zero except for a narrow range of ω. We denote by $\omega_{\min}$ and $\omega_{\max}$ the minimum and maximum $\cos \theta_s$ permitted by the size and location of the detector and sample surfaces. The directional distribution $g(\omega)$ corresponding to the geometric energy broadening of Fig. 15 is shown in Fig. 16.

3.3.3 Case of Arbitrary Orientation of Detector and Sample Planes
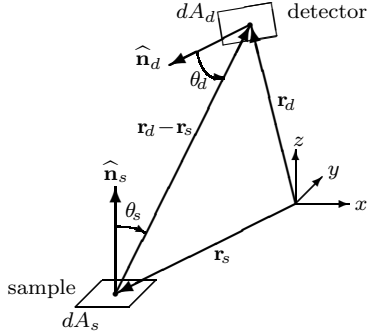
Figure 17. Two differential elements of area of the sample and detector surfaces with arbitrary orientation to each other.

Consider a differential element of area dA_s of the sample surface which has a unit normal $\widehat{\mathbf{n}}_s$ and is located at position $\mathbf{r}_s$ as shown in Fig. 17. A differential element of the detector surface dA_d has a unit normal $\widehat{\mathbf{n}}_d$ and is located at position $\mathbf{r}_d$. The probability an ion emitted isotropically from dA_s heads in a direction that intersects dA_d is

$$P_d = \frac{d\Omega_d}{4\pi} = \frac{dA_d \cos \theta_d}{4\pi |\mathbf{r}_d - \mathbf{r}_s|^2} = \frac{\widehat{\mathbf{n}}_d \bullet (\mathbf{r}_s - \mathbf{r}_d)}{4\pi |\mathbf{r}_d - \mathbf{r}_s|^3} dA_d. \tag{41}$$

Here $d\Omega_d$ is the solid angle subtended by the detector surface element dA_d at the sample element dA_s. The cosine of the emission angle $\omega_s \equiv \cos \theta_s$ is given by

$$\omega_s(\mathbf{r}_s, \mathbf{r}_d) = \frac{\widehat{\mathbf{n}}_s \bullet (\mathbf{r}_d - \mathbf{r}_s)}{|\mathbf{r}_d - \mathbf{r}_s|}. \tag{42}$$

If ν denotes the number of ions emitted per unit sample surface area, the number of ions emitted from dA_s in unit cosine about ω and that reach dA_d is

$$dN(\omega) = \nu \, dA_s \frac{\widehat{\mathbf{n}}_d \bullet (\mathbf{r}_s - \mathbf{r}_d)}{4\pi |\mathbf{r}_d - \mathbf{r}_s|^3} \delta(\omega - \omega_s(\mathbf{r}_s, \mathbf{r}_d)) dA_d. \tag{43}$$

Integration of this result over the detector and sample surfaces then gives the number of ions emitted in unit cosine about ω from the sample that reach the detector as

$$N(\omega) = \nu \int_{A_s} dA_s \int_{A_d} dA_d \frac{\widehat{\mathbf{n}}_d \bullet (\mathbf{r}_s - \mathbf{r}_d)}{4\pi |\mathbf{r}_d - \mathbf{r}_s|^3} \delta(\omega - \omega_s(\mathbf{r}_s, \mathbf{r}_d)). \tag{44}$$

Finally, division by the total number of ions born at depth t gives the probability distribution function $g(\omega) \equiv g(\cos \theta)$ that an ion reaching the detector leaves the sample in unit cosine about direction ω, namely

$$g(\omega) = N(\omega)/\nu A_s. \tag{45}$$

If the detector and source planes are parallel, then $\theta_s = \theta_d$ and Eq. (44) becomes the same as Eq. (39). An example of a directional distribution function is shown in Fig. 18.

18
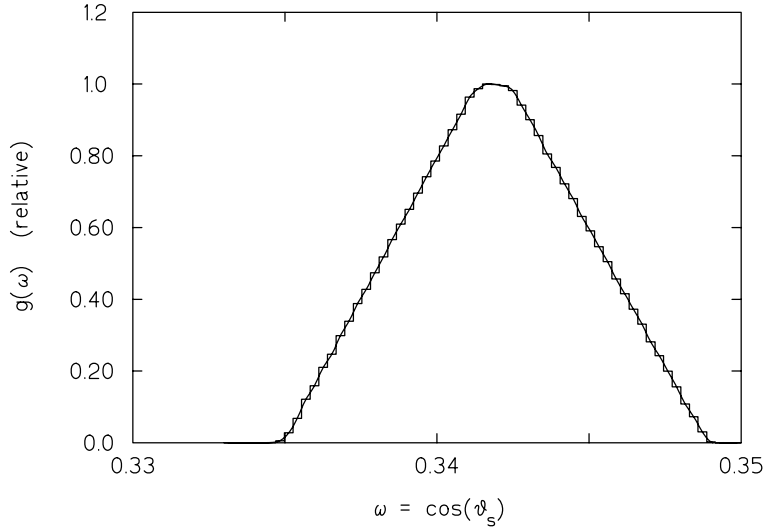
Figure 18. An example probability distribution for the emission direction $g(\omega)$. This result is for the example given by Croakley et al. [1995]. The detector is a 2.5-mm radius disk, the detector a 0.1-cm × 0.8-cm rectangle rotated by 70 degrees from the sample normal. The long edge of the detector is perpendicular the rotation plane, and the detector plane is perpendicular to the line between the sample and detector centers.

3.4 Importance of the Different Energy Broadening Effects

If we assume that all energy broadening effects can be adequately described by Gaussian-like behaviors, then the probability an ion born at depths in dt about $t = s\cos\theta_s$ is recorded by the spectrometer as having an energy in dE about E is

$$\mathcal{R}(\overline{E}(s), E)\, dE = \frac{1}{\sqrt{2\pi}\sigma(s)} \exp\left[-\frac{(\overline{E}(s) - E)^2}{2\,\sigma^2(s)}\right], \tag{46}$$

where $\sigma(s)$ is the standard deviation of all the energy broadening effects for an ion with path length s in the sample. If $\sigma_k(s)$ is the standard deviation of the kth broadening effect, then

$$\sigma(s) = \sqrt{\sum_k \sigma_k^2(s)}. \tag{47}$$

In practice, only energy straggling and the detector energy broadening effects are well described by a Gaussian model. The energy broadening caused by the geometry effect is decidedly non-Gaussian and must be treated explicitly (see the next section). However, in many practical cases the geometry effect can be ignored compared to the other two energy broadening effects. In this example we give a comparison of the importance of the three effects.

Estimates for KSU's NDP facility have been made for σ_{strag} as described in Section 3.1 and for σ_{geom} as calculated from Eq. (37) for alpha particles born at different depths in silicon. However, only the a single experiment result for σ_{det} has been made using a 1.47-MeV alpha particle. The fits to the MCA data shown in Fig. 12 yield values for $\sigma_{det} \simeq 19.0$ keV. How this values varies as the energy of the alpha particle changes is presently unknown. Thus, for lack of other data, we assume $\sigma_{det} = 19$ keV for alpha particles emitted at all depths in the sample.

The variation of σ_{det} with sample depth for α_2 particles from the ${}^{10}\text{B}(n,\alpha){}^7\text{Li}$ reaction is shown in Fig. 19 along with the variation of its components.
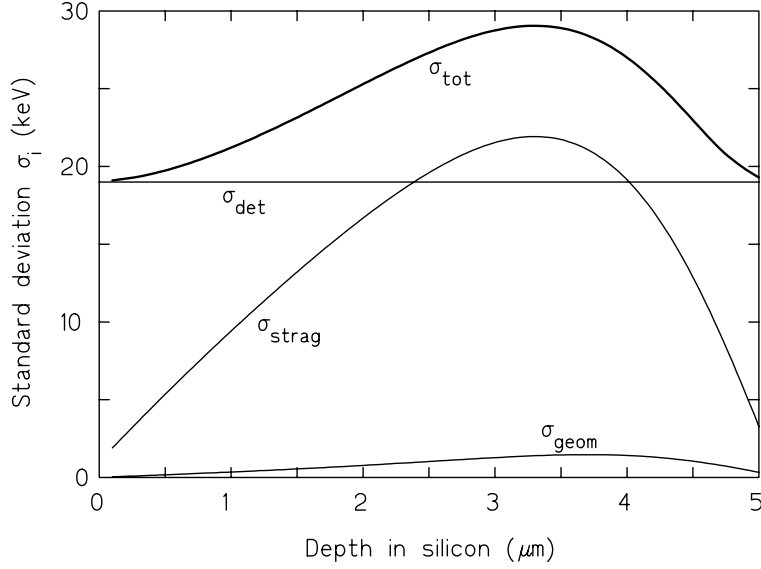
Figure 19. The various contributions to the total standard deviation of the energy broadening mechanisms for alpha particles in a typical NDP system.

3.5   NDP Spectra with Energy Broadening

The probability an ion born at depth x in the sample is emitted in $d\omega$ about direction $\omega \equiv \cos\theta$ with respect the surface normal that intersects the detector surface is denoted by $g(\omega)$ (see Sections 3.3.1 and 3.3.3). Because the depth x is almost always negligible compared to the sample-detector separation distance, this distribution is independent of x [Coakley et al. 1995].

Ions emitted at depth x in direction ω (see Fig. 5) travel a path length $s = x/\omega$ in the sample material and reach the detector with a mean residual energy $\overline{E}(s)$. If we assume a Gaussian model for energy broadening from both energy straggling and detector effects, the probability such an ion is recorded with energy in dE about E is

$$\mathcal{R}(E, \overline{E}(s), \sigma(s)) \, dE = \frac{1}{\sqrt{2\pi}\sigma(s)} \exp\left[-\frac{(E - \overline{E}(s))^2}{2\,\sigma^2(s)} \right] dE, \tag{48}$$

where $\sigma^2(s) = \sigma_{det}^2 + \sigma_{strag}^2$. With this energy broadening model, the probability $p(x, E) \, dE$ that an ion born at depth x in the sample is recorded with an energy in dE about E is

$$p(x, E) \, dE = \left[\int_{\omega_{\min}}^{\omega_{\max}} g(\omega) \mathcal{R}(E, \overline{E}(x/\omega), \sigma(x/\omega)) \, d\omega \right] dE. \tag{49}$$

If $C(x)$ denotes the concentration at depth x of the trace isotope that produces the ion, then from Eq. (7) the number of ions produced in dx about x is

$$N_{ion}(x) \, dx = F_{ion}(x) \, \Delta V = C(x) \, f_{ion}\overline{\sigma}_{ion} \, \Phi_t \left(\frac{A_n}{\cos\theta_n} \right) dx = \widehat{\kappa} \, C(x) \, dx, \tag{50}$$

where the thermal neutron fluence incident on the sample in measurement time Δt is $\Phi_t = \phi_t \Delta t$, and $\widehat{\kappa} \equiv f_{ion}\overline{\sigma}_{ion} \, \Phi_t A_s$ since $A_s = A_n/\cos\theta_n$.

20

With the results of Eqs. (49) and (50), the number of ions born at depths dx about x and subsequently recorded by the MCA with energies in dE about E is

$$dy(E)\,dE = [N_{ion}(x)\,dx]\,p(x,E)\,dE = \widehat{\kappa}C(x)\,dx\,p(x,E)\,dE. \tag{51}$$

The number born at all depths that are recorded with energies in dE about E is thus

$$y(E) = \widehat{\kappa}\int_0^{x_{\max}} C(x)p(x,E)\,dx. \tag{52}$$

Finally, the number of counts recorded in bin i of the MCA energy spectrum (bin width 2Δ and midpoint energy E_i) is

$$y_i = \int_{E_i-\Delta}^{E_i+\Delta} y(E)\,dE = \widehat{\kappa}\int_0^{x_{\max}} dx\,C(x)\int_{E_i-\Delta}^{E_i+\Delta} dE\,p(x,E). \tag{53}$$

This may be written as

$$\boxed{y_i = \int_0^{x_{\max}} C(x)R_i(x)\,dx} \qquad i = 1,\ldots,N, \tag{54}$$

where the *channel response function* is defined as

$$R_i(x) = \widehat{\kappa}\int_{E_i-\Delta}^{E_i+\Delta} dE\,p(x,E)$$

$$= \widehat{\kappa}\int_{\omega_{\min}}^{\omega_{\max}} d\omega\,g(\omega)\int_{E_i-\Delta}^{E_i+\Delta} dE\,\mathcal{R}(E,\overline{E}(x/\omega),\sigma(x/\omega))$$

$$= \widehat{\kappa}\int_{\omega_{\min}}^{\omega_{\max}} d\omega\,g(\omega)W_i(x/\omega). \tag{55}$$

Here the so-called *spread function* $W_i(x/\omega)$ is defined as

$$W_i(s) \equiv \int_{E_i-\Delta}^{E_i+\Delta} dE\,\mathcal{R}(E,\overline{E}(s),\sigma(s))$$

$$= \frac{1}{2}\left[\text{erf}\left(\frac{E_i+\Delta-\overline{E}(s)}{\sqrt{2}\,\sigma(s)}\right) - \text{erf}\left(\frac{E_i-\Delta-\overline{E}(s)}{\sqrt{2}\,\sigma(s)}\right)\right]. \tag{56}$$

Special case of Good Geometry: In many NDP facilities, the geometry for obtaining the MCA ion-energy spectrum is such that energy spreading from the geometry effect is very small compared to energy straggling and detector resolution effects. See, for example, the KSU NDP results of Fig. 19. In such cases, the direction distribution function $g(\omega)$ can be approximated by a delta function, i.e., $g(\omega) \simeq \delta(\omega-\omega_s)$ where ω_s is the angle between the sample normal and the ray between the centers of the sample and detector (see Fig. 14). Under this approximation

$$R_i(x) \simeq \widehat{\kappa}\int_{\omega_{\min}}^{\omega_{\max}} \delta(\omega-\omega_s)\,W_i(x/\omega)\,d\omega = \widehat{\kappa}W_i(x/\omega_s)$$

$$= \frac{\widehat{\kappa}}{2}\left[\text{erf}\left(\frac{E_i+\Delta-\overline{E}(x/\omega_s)}{\sqrt{2}\,\sigma(x/\omega_s)}\right) - \text{erf}\left(\frac{E_i-\Delta-\overline{E}(x/\omega_s)}{\sqrt{2}\,\sigma(x/\omega_s)}\right)\right]. \tag{57}$$

Example response functions are shown in Figs. 20 and 21.
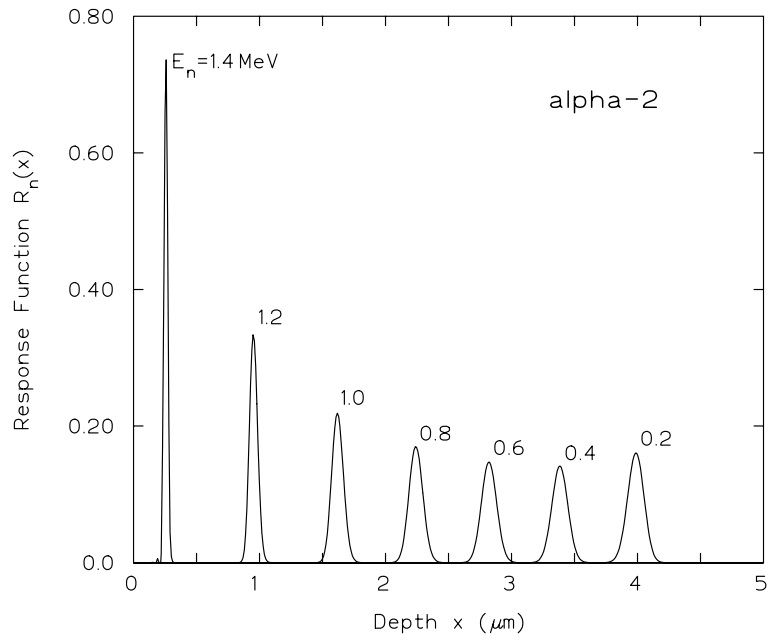
Figure 20. The MCA channel response function for the 1.4721-MeV α particle of the ^{10}B(n,α)^{7}Li reaction in a silicon sample. Only the energy straggling component of energy broadening is considered.
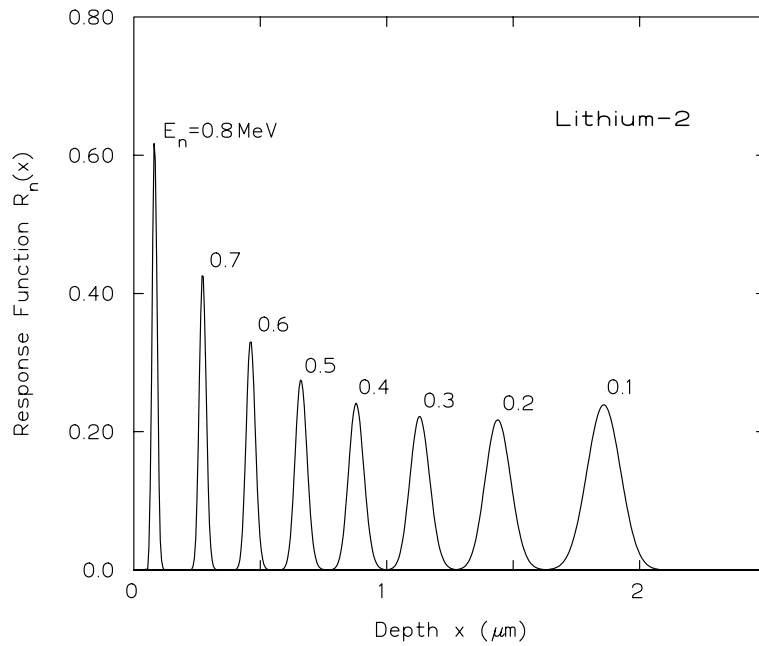
Figure 21. The MCA channel response function for the 0.8398-MeV lithium ion of the ^{10}B(n,α)^{7}Li reaction in a silicon sample. Only the energy straggling component of energy broadening is considered.

3.6 Numerical Evaluation of the MCA Ion Energy Spectrum

Both for comparison to experimental data with NDP standards samples and for testing deconvolution or unfolding techniques to obtain the concentration profile $C(x)$ from the MCA spectral data, it is important to be able to compute the expected MCA spectrum for a specified profile. In this section we discuss several algorithms for this spectrum construction.

The expected number of counts in channel i of the MCA spectrum is given by Eq. (54). This integral can be approximated by an appropriate weighted sum of concentrations at discrete depths in the sample by using some quadrature approximation for the integral. Suppose we are given the concentration at M equispaced depths x_j such that $x_1 = 0$ and $x_M = x_{\max}$, the depth beyond which an ion cannot escape the sample. The concentration at depth x_j is denoted by $c_j \equiv C(x_j)$. With this discrete spatial grid, Eq. (54) is decomposed into a sum of integrals over the subintervals as

$$y_i = \int_0^{x_{\max}} dx \, R_i(x)C(x) = \sum_{j=1}^{M-1} \int_{x_j}^{x_{j+1}} dx \, R_i(x)C(x). \tag{58}$$

Each integral in Eq. (58) is then evaluated by numerical quadrature to express the integrals in term of the c_j. The resulting linear equations can be written as

$$y_i = \sum_{j=1}^{M} R_{ij}c_j, \quad i = 1, ..., N \tag{59}$$

or in matrix notation

$$\mathbf{y} = \mathbf{R \cdot c}. \tag{60}$$

This result represents N equations in the M unknowns $\{c_j\}$. Here the $N \times M$ matrix $\mathbf{R}$ depends on the numerical quadrature approximation selected to evaluate Eq. (58). Three possible schemes are presented below.

3.6.1 An Interval-Average Approximation

In this discretization, $C(x)$ in each of the subintervals is approximated by the average of its endpoint values. Thus Eq. (58) becomes

$$
\begin{aligned}
y_i \quad &\simeq \quad \sum_{j=1}^{M-1} \frac{c_{j+1} + c_j}{2} \int_{x_j}^{x_{j+1}} R_i(x) \, dx \\
&= \quad \sum_{j=1}^{M-1} \frac{c_{j+1} + c_j}{2} Q_{i,j} \\
&\equiv \quad \sum_{j=1}^{M} R_{ij}c_j
\end{aligned}
\tag{61}
$$

where the elements of the $\mathbf{R}$ matrix are given by

$$R_{ij} = \frac{1}{2} \begin{cases} Q_{i,1}, & j = 1 \\ Q_{i,j-1} + Q_{i,j}, & j = 2, \dots, M-1 \\ Q_{i,M-1}, & j = M \end{cases} \tag{62}$$

and

$$Q_{i,j} \equiv \int_{x_j}^{x_{j+1}} R_i(x)\, dx.$$

The evaluation of $Q_{i,j}$ generally must be performed numerically.

3.6.2 A Piece-Wise Linear Approximation

In this approximation we assume $C(z)$ varies linearly between its values at the endpoints of each subinterval, i.e.,

$$C(x) \simeq (x_{j+1} - x)c_j/\Delta_j + (x - x_j)c_{j+1}/\Delta_j, \quad x_j \leq x \leq x_{j+1}, \tag{63}$$

where $\Delta_j \equiv (x_{j+1} - x_j)$. Substitution of this linear approximation into Eq. (58) gives Eq. (59) where the R_{ij} are given by

$$R_{ij} = \begin{cases} \displaystyle\int_{x_1}^{x_2} dz\, f_1(x) R_i(x), & j = 1 \\[3ex] \displaystyle\int_{x_{j-1}}^{x_{j+1}} dx\, f_j(x) R_i(x), & j = 2, \ldots, M-1 \\[3ex] \displaystyle\int_{x_{M-1}}^{x_M} dx\, f_M(x) R_i(x), & j = M \end{cases} \tag{64}$$

where the weighting functions $f_j(x)$ are defined as

$$f_j(x) = \begin{cases} (x - x_{j-1})/\Delta_{j-1}, & x_{j-1} \leq x < x_j \\[1ex] (x_{j+1} - x)/\Delta_j, & x_j \leq x < x_{j+1} \\[1ex] 0, & \text{otherwise.} \end{cases} \tag{65}$$

The integrals in Eq. (64) generally must be evaluated using numerical integration.

3.6.3 A Piece-Wise Quadratic Approximation

Equation (54) can also be approximated by

$$y_i = \int_0^{x_{\max}} dx\, R_i(x) C(x) = \sum_{j=1}^{M-2}{}' \int_{x_j}^{x_{j+2}} dx\, R_i(x) C(x), \tag{66}$$

where the prime on the summation indicates that the summation is over only odd values of j. For the approximation developed here, M is assumed odd. Now approximate $C(x)$ in each pair of adjacent subintervals by a quadratic function. For equally spaced nodes with $\Delta = x_{j+1} - x_j$, $C(x)$ in interval (x_j, x_{j+2}) is approximated by

$$C(x) \simeq \frac{(x - x_{j+1})(x - x_{j+2})}{2\Delta^2} c_j - \frac{(x - x_j)(x - x_{j+2})}{\Delta^2} c_{j+1} + \frac{(x - x_j)(x - x_{j+1})}{2\Delta^2} c_{j+2}. \tag{67}$$

24

Substitution of this result into Eq. (66) gives Eqs. (59) where the R_{ij} are now given by

$$R_{ij} = \frac{1}{2\Delta^2} \begin{cases} \displaystyle\int_{x_1}^{x_3} dx\,(x-x_2)(x-x_3)R_i(x), & j=1 \\[2ex] \displaystyle\int_{x_{j-2}}^{x_j} dx\,(x-x_{j-2})(x-x_{j-1})R_i(x) \\[1ex] \quad + \displaystyle\int_{x_j}^{x_{j+2}} dx\,(x-x_{j+1})(x-x_{j+2})R_i(x), & j \text{ odd}, \ j\neq 1, M \\[2ex] -2\displaystyle\int_{x_{j-1}}^{x_{j+1}} dx\,(x-x_{j-1})(x-x_{j+1})R_i(x), & j \text{ even} \\[2ex] \displaystyle\int_{x_{M-2}}^{Z_M} dx\,(x-x_{M-2})(x-x_{M-1})R_i(x), & j=M \end{cases} \tag{68}$$

3.7 Examples of Reconstructed MCA Spectra

In Fig. 22 two 256-channel MCA ion spectra are shown for NIST's SRM-2137 ^{10}B implanted sample. The spectrum with energy straggling, but without any geometric energy broadening, was calculated from Eq. (59) using the interval average approximation of Section 3.6.1 with $M = 65$ equispaced x_j between $x = 0$ and 0.320 μm (the values at which NIST tabulates the ^{10}B concentration). Notice that for this example, energy straggling is negligible since all the ^{10}B is within 0.32 μm of the sample surface and, for such depths, energy straggling is negligible as can be seen from the extreme narrowness of the α_2 response function in Fig. 20 for $x < 0.3$ μm.

Another possible NDP profile problem is to analyze a sample with a constant ^{10}B concentration throughout the sample. Such, for example would be a sample of Pyrex (borosilicate) glass. In Fig. 23 two predicted MCA ion-energy spectra are shown, one for a constant ^{10}B concentration at all depths and a second for the case the ^{10}B is constrained to a sublayer between 1 and 2.5 μm below the surface and zero otherwise. Energy straggling is apparent in this second spectrum as evidenced by a more gradual drop off of the α_2 component around 0.9 MeV compared to its abrupt rise around 1.4 MeV. Both spectra were also calculated from Eq. (59) using the interval average approximation of Section 3.6.1 with $M = 400$ equispaced x_j between $x = 0$ and 6 μm.

4 The Unfolding Problem: Recovering the Concentration Profile

The observed counts in channel i of the ion energy spectrum is generally related to the concentration profile $C(x)$ by Eq. (54), i.e.,

$$y_i = \int_0^{x_{\max}} C(x)R_i(x)\,dx \quad i=1,\ldots,N, \tag{69}$$

where the *channel response function* $R_i(x)$ depends on the model used to predict the energy distribution of the ions reaching the detector. For the case of no energy broadening, this response function if given by Eq. (21). For the case of energy broadening described by a Gaussian distribution about the mean residual energy (see Section 3.5), the channel response function is given by Eq. (55) or by Eq. (57) if geometric effects can be ignored.
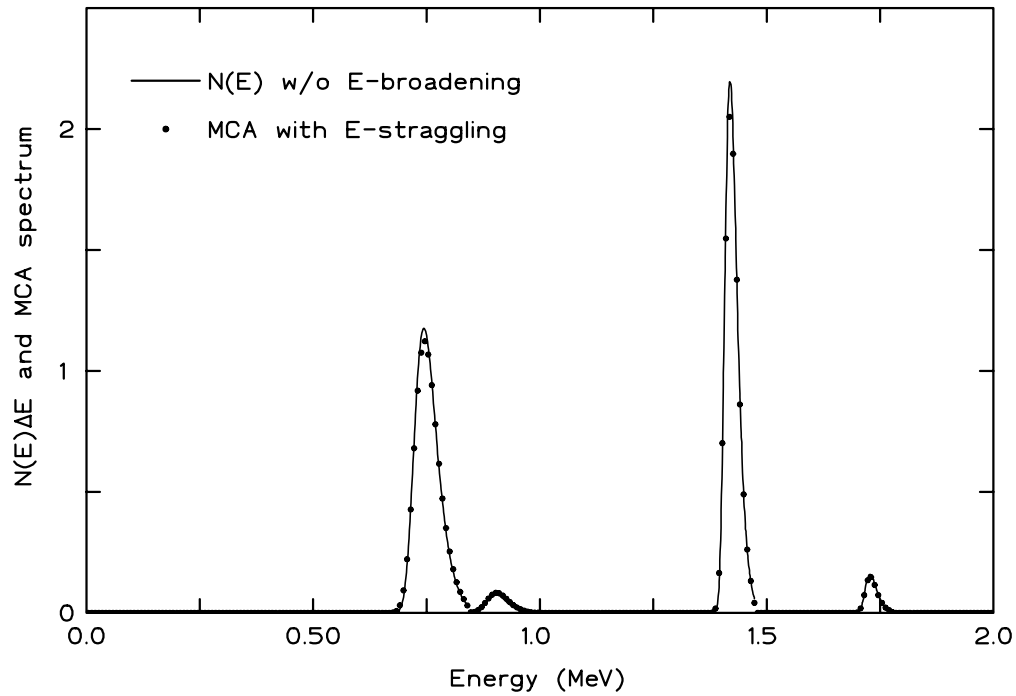
Figure 22. The MCA ion energy spectrum for NIST's SRM-2137 (see Fig. 6 for ^{10}B concentration profile) The line is the spectrum without any energy broadening (the same as shown in Fig. 7), and the circles show the spectrum with energy straggling included.
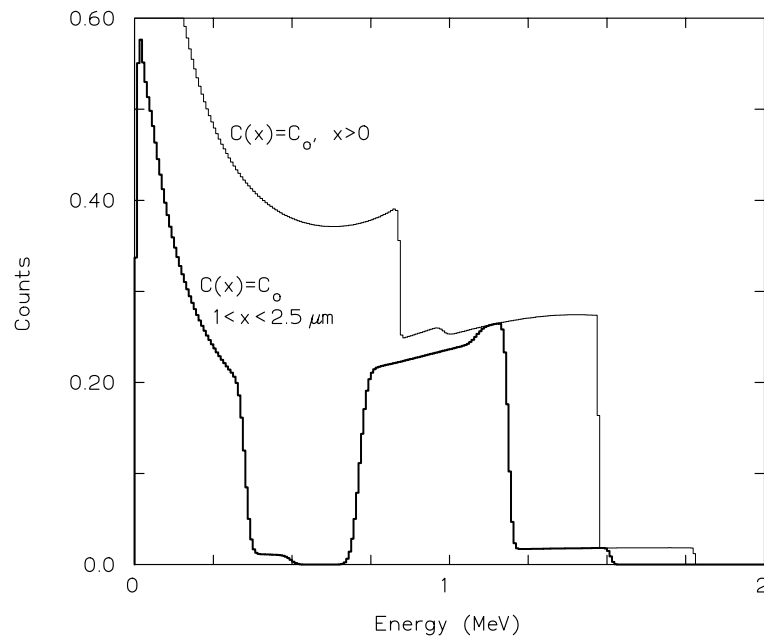
Figure 23. The predicted MCA ion spectrum for a sample with $C(x) = C_o$ for all x (light line), and for $C(x) = C_o$ only for $1 < x < 2.3$ μm.

The solution of Eq. (69) for the concentration profile is an inversion problem encountered in many diverse fields. For example, this same inversion problem, but with different kernels, is encountered in oil-well logging, neutron scattering, geophysical data analysis, atmospheric remote sensing, astrophysics, medical tomography, and many other data analysis applications. The solution of Eq. (69) for $C(x)$ given the N MCA channel counts y_i, however, is a very ill-posed problem since we can have an infinite number of unknown values of $C(x)$ between $x = 0$ and $x = x_{\max}$ and only a finite number of known y_i.

In most inversion schemes, the Fredholm integral equation of Eq. (69) is approximated by a set of M algebraic equations for the concentration at M equispaced discrete depths in the sample (see Section 3.6), namely

$$\boxed{y_i = \sum_{j=1}^{M} R_{ij} u_j, \quad i = 1, ..., N,} \tag{70}$$

where $u_j \equiv C(x_j)$ and the R_{ij} depend on the quadrature approximation used.[2] In matrix notation, these equations may be written as

$$\mathbf{y} = \mathbf{R} \cdot \mathbf{u}. \tag{71}$$

The inversion of Eqs. (70) generally has no unique solution since the number of unknowns M (the u_j) is most likely different from the number N of measured data (the y_i).

If $M < N$ (more equations than unknowns) the problem is over-determined and generally no solution exists. By contrast, if $M > N$ (more unknowns than equations) there is an infinity of solutions because the solution space (of dimension M) has an $(M - N)$ dimensional degeneracy, i.e., any $(M - N)$ components of $\mathbf{u}$ can be specified arbitrarily and still have Eq. (70) satisfied. This under-determined case is typical of an NDP spectrum that is concentrated in only a few MCA channels. The case with $M = N$, which has a unique solution, is very unlikely since selection of the MCA spectrum scale and the discretization of the concentration profile $C(x)$ are usually done independently.

The question on how to extract a meaningful estimate of the concentration profile from Eqs. (70) is the subject of this section. Two approaches are presented: (a) a least-squares fitting technique, and (b) a linear regularization technique. However, before we consider these approaches, we first consider the ideal case of Section 2.2 in which there is no energy broadening of the NDP spectrum.

4.1 Unfolding Techniques for the NDP Problem

Several different approaches have been applied to estimate the concentration profile $C(x)$ (or the $u_j \equiv C(x_j)$ from the measured MCA channel counts y_i.

4.1.1 Direct methods:

In this approach one attempts to describe the concentration profile by some known function $G(x; \boldsymbol{\xi})$ with M parameters ξ_i. For example, one might think that the concentration profile could be well approximated by a four-parameter beta function

$$G(x; A, \tau, \alpha, \beta) = C_o \frac{\Gamma(\alpha + \beta)}{\Gamma(\alpha)\Gamma(\beta)} \tau^{1 - \alpha - \beta} x^{\alpha - 1} (\tau - x)^{\beta - 1}, \quad 0 \le 0 \le \tau.$$

---

[2] In this section we use u_j instead of c_j to emphasize that the u_j are the *unknown* quantities we are seeking. Similarly we will use $u(x) \equiv C(x)$ to denote the continuous concentration profile in the sample.

The amplitude parameter C_o adjusts the magnitude of the profile and the positive shape parameters α and β allow this function to assume a wide variety of shapes over the interval $(0,\tau)$. Alternatively, one might assume the concentration profile is a piece-wise linear functions between M equidistance depths in the sample, as was done in Section 3.6.2. In this case, the unknown parameters are the concentrations u_i at each depth – the very quantities that we are seeking!

Once a concentration model has been selected, a predicted MCA spectrum $\widehat{y}_i, i = 1, ...N$ can be computed from Eq. (69) with C(x) replaced by the model $G(x; \boldsymbol{\xi})$. One then selects the "best" values for the model parameters $\boldsymbol{\xi}$ by minimizing the disagreement between the measured data and the predicted data. This is usually done by minimizing the statistic [Hoffman 1983]

$$\chi^2 = \sum_{i=1}^{N}(y_i - g_i)^2.$$

The direct approach often produces erratic results when there is significant noise in the data or if there is a large number of parameters to be estimated. However, it is this approach we shall study in the following sections.

4.1.2 Iterative Methods:

Several iterative techniques have been used for unfolding MCA energy spectral data. Many are *ad hoc* schemes whose mathematical properties, such as convergence, are not well established. Nevertheless, they often produce useful results, especially if the concentration profile is a slowly varying function of x. We illustrate this approach with a simple iterative scheme proposed long ago by Cittert [1931] and used for NDP analysis by Maki et al. [1986].

This scheme is based on the formulation of Eq. (70), and with it a successive series of estimates $u_i^{(n)}, n = 1, ...$ is obtained for the concentration u_i. From Eq. (70), the error between the true value and the nth estimate is

$$e_i^{(n)} \equiv y_i - \sum_{j=1}^{M} R_{ij}u_j^{(n)} \tag{72}$$

A revised estimate of u_i is obtained by adding this error term to the previous estimate, i.e.,

$$u_i^{(n+1)} = u_i^{(n)} + \left[y_i - \sum_{j=1}^{M} R_{ij}u_j^{(n)} \right], \quad n = 0, 1, ... \tag{73}$$

In this scheme we see that if $u_j^{(n)}$ is too large (or small) the error is negative (or positive) and a corrector is thus subtracted (or added) to obtain the next estimate. The iteration is begun with $u_i^{(0)} = y_i$. After several iterations the error term consists mostly of noise, indicated by random sign changes in $e_i^{(n)}$ as i varies. The final estimate, after k iterations, is then obtained by "smoothing" out the noise as [Wertheim 1975]

$$u_j^{est} = u_j^{(k)} - k \left[y_i - \sum_{j=1}^{M} R_{ij}u_j^{(k)} \right]. \tag{74}$$

Critical to the success of this procedure is that both the data y_i and the concentration profile be smooth and slowly varying.

28

4.1.3 Fourier Transform Methods

In Eq. (70) the response matrix elements R_{ij} are narrowly peaked around $i \simeq j$, i.e., R_{ij} is large when the residual energy from depth j is near the MCA channel energy E_i. Thus Eq. (70) can be viewed as a discrete convolution of a signal $u(x)$ with a narrowly peaked response function. Using the convolution theorem for Fourier transforms [Press et al. 1992], the discrete Fourier transform of the u_j can be obtained in terms of the discrete Fourier transforms of y_i and R_{ij}. Inversion then gives an estimate of u_j.

The difficulty with Fourier transform techniques is that spurious features are often added to the unfolded profile as a result of aliasing errors produced by the relatively small amount of discrete data in the MCA spectrum.

4.2   Least-Squares: Over-Determined Set of Equations

For the case in which we have more data than unknowns, the usual procedure is to seek a solution vector $\mathbf{u}$ that minimizes the difference between the data $\mathbf{y}$ and the MCA spectrum predicted by the NDP model. This difference between a model and measured data is often quantified by the χ^2 statistic, namely,

$$\chi^2 = \sum_{i=1}^{N} \sum_{j=1}^{M} \left[y_i - \sum_{k=1}^{M} R_{ik} u_k \right] S_{ij}^{-1} \left[y_j - \sum_{k=1}^{M} R_{jk} u_k \right] \tag{75}$$

$$\simeq \sum_{i=1}^{N} \frac{1}{\sigma_i^2} \left[y_i - \sum_{k=1}^{M} R_{ik} u_k \right]^2 = |\mathbf{A} \cdot \mathbf{u} - \mathbf{b}|^2. \tag{76}$$

Here $S_{ij} = \text{Covar}[n_i, n_j]$ are the elements of the covariance matrix. The approximate equality in the above result holds if we can neglect the off-diagonal covariance terms, with $\sigma_i^2 = \text{Covar}[n_i, n_i]$. The matrix $\mathbf{A}$ has elements $A_{ij} = R_{ij}/\sigma_i$ and the vector $\mathbf{b}$ has elements $b_i = y_i/\sigma_i$. For the counting data of a MCA spectrum, the estimate of σ_i is $\sqrt{y_i}$ provided y_i is sufficiently large (namely, $y_i \gtrsim 20$).

The problem of finding the best agreement between the data and model is to find the vector $\mathbf{u}$ that minimizes this $\chi^2(\mathbf{y})$ statistic. Should we find a $\mathbf{u}$ such that $\chi^2 = 0$, then this is a "perfect" solution giving exact agreement between experiment and the model. However, such a solution seldom exists, particularly when the y_i usually contain some random noise. The best we can do is to find a $\mathbf{u}$ that minimizes $\chi^2(\mathbf{y})$. Such a solution is often called the *least-squares solution* since it minimizes the (weighted) sum of the squares of the differences between the data and model.

4.2.1   Least-Squares Solution

To obtain the least-squares solution, we seek the vector $\mathbf{u}$ that minimizes the χ^2 of Eq. (76) which can be written as

$$\chi^2 = \sum_{i=1}^{N} \frac{1}{\sigma_i^2} \left[y_i - \sum_{j=1}^{M} R_{ij} u_j \right]^2. \tag{77}$$

At the minimum, $\partial \chi^2 / \partial u_k = 0$. Differentiating the above equation gives

$$\frac{\partial \chi^2}{\partial u_k} = 0 = \sum_{i=1}^{N} \frac{2}{\sigma_i^2} \left[y_i - \sum_{j=1}^{M} R_{ij} u_j \right] R_{ik}, \quad k = 1, \ldots, M, \tag{78}$$

which gives

$$\sum_{j=1}^{M}\sum_{i=1}^{N}\frac{R_{ij}R_{ik}}{\sigma_i^2}u_j = \sum_{i=1}^{N}\frac{y_iR_{ik}}{\sigma_i^2}, \quad k = 1, \ldots, M. \tag{79}$$

These so-called *normal equations* can be written more compactly as

$$\sum_{j=1}^{M}\alpha_{kj}u_j = \beta_k, \quad k = 1, \ldots, M, \tag{80}$$

where

$$\alpha_{kj} \equiv \sum_{i=1}^{N}\frac{R_{ij}R_{ik}}{\sigma_i^2} \qquad \text{and} \qquad \beta_k \equiv \sum_{i=1}^{N}\frac{y_iR_{ik}}{\sigma_i^2}. \tag{81}$$

The normal equations, in matrix form, are thus

$$\boldsymbol{\alpha} \cdot \mathbf{u} = \boldsymbol{\beta}, \tag{82}$$

where the $M \times M$ matrix $\boldsymbol{\alpha} = \mathbf{A^T} \cdot \mathbf{A}$ and the M-component vector $\boldsymbol{\beta} = \mathbf{A^T} \cdot \mathbf{b}$.

Formally, the solution of Eqs. (82) can be written as

$$u_k = \sum_{k=1}^{M}\alpha_{jk}^{-1}\beta_k = \sum_{k=1}^{M}\alpha_{jk}^{-1}\left[\frac{y_iR_{ik}}{\sigma_i^2}\right]. \tag{83}$$

In practice, rather than generate the inverse matrix $\boldsymbol{\alpha}^{-1}$, one solves the normal equations (Eqs. (82)) directly. However, as Price et al. [1992] points out, the solution of these linear equations is very susceptible to numerical roundoff errors and often the solution $\mathbf{u}$ obtained with, say, Gauss elimination is often meaningless with adjacent components oscillating between enormous positive and negative values. The reason for this is that the normal equations are often nearly singular because different combinations of the R_{ij} response matrix elements often fit the data equally well (or equally poorly). Consequently, the $\boldsymbol{\alpha}$ matrix, unable to distinguish between nearly equal combinations, becomes close to singular.

To avoid such spurious solutions of the normal equations, a different approach to finding the minimum of χ^2 should be used. This approach is to perform the minimization using the *singular value decomposition* (SVD) technique. The algorithms and theory for this method are presented by Price et al. [1992] and will not be repeated here. The solution that minimizes χ^2 of Eq. (77) is readily obtained with the subroutine `svdfit` presented by Price et al. [1992]. As an added bonus, this SVD method for minimizing χ^2 can also be used for under-determined sets of equations!

4.3   Linear Regularization: Under-Determined Set of Equations

Minimization of the positive functional $\mathcal{A}[\mathbf{u}] \equiv \chi^2 = |\mathbf{A} \cdot \mathbf{u} - \mathbf{b}|^2$ for a matrix $\mathbf{A}$ that is degenerate, i.e., has fewer rows than columns, will not give a unique solution for $\mathbf{u}$. To obtain a unique solution, additional constraints must be imposed on the minimization problem. For example, if any non-degenerate strictly convex functional $\mathcal{B}[\mathbf{u}]$, for example $\mathbf{u}^T \cdot H \cdot \mathbf{u}$, is added, then the minimization of $\mathcal{A}[\mathbf{u}] + \lambda\mathcal{B}[\mathbf{u}]$ *will* produce a unique solution $\mathbf{u}$ [Press et al. 1992]. The addition of the term $\lambda\mathcal{B}[\mathbf{u}]$ is said to "regularize" the minimization problem, i.e., to produce a unique solution.

Thus in the inverse problem, to obtain a unique solution for $\mathbf{u}$, one solves the following minimization problem

$$\text{minimize:} \quad \mathcal{A}[\mathbf{u}] + \lambda\mathcal{B}[\mathbf{u}]. \tag{84}$$

This is the central principle of inversion theory. As the Lagrange multiplier λ varies from 0 to ∞, the unique solution $\mathbf{u}$ varies from one minimizing $\mathcal{A}[\mathbf{u}]$ to one minimizing $\mathcal{B}[\mathbf{u}]$. To obtain the "best" solution (corresponding to a particular value of λ) one must choose a particular criterion. For example, one might pick λ so that $\chi^2 = N$ to agree with the expected value of χ^2. Alternatively, one might pick λ purely subjectively so as to produce, for example, a "smooth" solution or a solution sensitive to abrupt changes in the profile $u(x)$. Finally, for simulated NDP data obtained by accurate numerical integration of Eq. (58), the most accurate inversion will be obtained with λ made as small as possible, but still large enough to avoid numerical instabilities in the minimization algorithm.

The many apparently different approaches used for inversion problems by the regularization technique all involve minimizing the functional of Eq. (84) with the choice for $\mathcal{A}[\mathbf{u}]$ and $\mathcal{B}[\mathbf{u}]$ dependent on the problem and the inversion philosophy. Such methods include the Backus-Gilbert and Maximum Entropy methods. These are not reviewed here; the interested reader is referred to Price et al. [1992]. Rather I have found the *linear regularization*, the simplest of these regularization techniques, to be effective for the NDP unfolding problem. In essence this approach imposes a smoothness constraint on the solution. The linear regularization method and a *constrained linear regularization* approach are discussed in the following subsections.

4.3.1 The Linear Regularization (LR) Method

The linear regularization method goes by many names, for example, Tikhonov-Miller regularization [Tikhonov 1964; Tikhonov and Arsenin 1977; Miller 1970; Biemond et al. 1990], the Phillips-Twomey method [Phillips 1962; Twomey 1963], the constrained linear inversion method [Twomey 1977], and the method of regularization [Craig and Brown 1986].). As with any method that has evolved from many different disciplines, the notation and ideas in the many seminal works are often quite different. In the summary of this and the other inversion methods discussed in this paper, we adhere closely to the notation of Press et al. [1992].

In the linear regularization approach, the functional $\mathcal{A}[\mathbf{u}]$ of Eq. (84) is taken as the χ^2 of Eq. (76), i.e., $\mathcal{A}[\mathbf{u}] = |\mathbf{A} \cdot \mathbf{u} - \mathbf{b}|^2$, and the functional $\mathcal{B}[\mathbf{u}]$ is chosen as some measure of the smoothness of $u(x)$, which is derived from first or higher derivatives of $u(x)$. In particular, the linear regularization method requires that $\mathcal{B}[\mathbf{u}] = \mathbf{u}^T \cdot \mathbf{H} \cdot \mathbf{u}$ where $\mathbf{H}$ is some appropriate symmetric smoothing matrix. The inversion solution is thus determined by the following minimization problem:

$$\text{minimize:} \quad \mathcal{A}[\mathbf{u}] + \lambda \mathcal{B}[\mathbf{u}] = |\mathbf{A} \cdot \widehat{\mathbf{u}} - \mathbf{b}|^2 + \lambda \mathbf{u}^T \cdot \mathbf{H} \cdot \mathbf{u}. \tag{85}$$

The matrix $\mathbf{H}$ is obtained by making some *a priori* assumption about the nature of the concentration profile $C(x) \equiv u(x)$. Several example *smoothing* matrices are presented in Section 4.3.2 below.

To obtain the minimum of the functional of Eq. (85) and find $\mathbf{u}$, we write Eq. (85) in its component form as

$$\mathcal{F}[\mathbf{u}] \equiv \mathcal{A}[\mathbf{u}] + \lambda \mathcal{B}[\mathbf{u}] = \sum_{i=1}^{N} \left[\sum_{j=1}^{M} A_{ij} u_j - b_i \right]^2 + \lambda \sum_{i=1}^{M} u_i \sum_{j=1}^{M} H_{ij} u_j. \tag{86}$$

The values of u_j that minimize this functional are the solutions of the M *normal equations* obtain by setting the derivative of $\mathcal{F}[\mathbf{u}]$ with respect to u_j to zero. Differentiation of Eq. (86) with respect to u_j, setting the result to zero, and use of the symmetry property of $\mathbf{H}$ gives

$$\sum_{j=1}^{M} \left\{ \left(\sum_{i=1}^{N} A_{ik} A_{ij} \right) + \lambda H_{kj} \right\} u_j = \sum_{i=1}^{N} A_{ik} b_i, \quad k = 1, ..., M, \tag{87}$$

or, in matrix form,

$$(\mathbf{A}^T\boldsymbol{\cdot}\mathbf{A} + \lambda\mathbf{H})\boldsymbol{\cdot}\mathbf{u} = \mathbf{A}^T\boldsymbol{\cdot}\mathbf{b}. \tag{88}$$

This set of M linear algebraic equations is readily solved for $\mathbf{u}$ using standard techniques such as the Lower-Upper (LU) decomposition method or the Singular Value Decomposition (SVD) method [Press et al. 1992].

Notice that before solving Eq. (88), one must first pick a value of λ. What value to pick? If the errors σ_i are known reasonably well, one might pick λ so that the χ^2 equals N. To obtain confidence bounds on u, λ could be chosen so that χ^2 equals $N \pm (2N)^{1/2}$. Thus the solution of Eq. (88) involves a root finding process whereby λ is adjusted until χ^2 attains some prescribed value. As a starting point for the λ search, Press et al. [1922] suggests

$$\lambda = \mathrm{Tr}(\mathbf{A}^T\boldsymbol{\cdot}\mathbf{A})/\mathrm{Tr}(\mathbf{H}) \tag{89}$$

where Tr is the matrix trace (sum of diagonal elements).

4.3.2 Smoothing Matrices

The construction of the $M \times M$ matrix $\mathbf{H}$ depends on the *a priori* smoothness criterion chosen. For example, if we believe that the concentration profile $u(x)$ is approximately constant, then a reasonable functional to minimize so as to enforce this belief is (assuming equispaced values of x_j)

$$\mathcal{B}[\mathbf{u}] \propto \int_0^\infty [\hat{u}'(x)]^2 \, dx \ \propto \sum_{j=1}^{M-1} [\hat{u}_j - \hat{u}_{j+1}]^2 \tag{90}$$

since this functional is nonnegative and vanishes only when $\hat{u}(x)$ equals a constant. The constant of proportionality can be absorbed into the parameter λ so that the discretized form of $\mathcal{B}[\mathbf{u}]$ can be written as

$$\mathcal{B}[\mathbf{u}] = |\mathbf{B}\boldsymbol{\cdot}\hat{\mathbf{u}}|^2 = \hat{\mathbf{u}}^{\mathbf{T}}\boldsymbol{\cdot}(\mathbf{B}^T\boldsymbol{\cdot}\mathbf{B})\boldsymbol{\cdot}\hat{\mathbf{u}} = \hat{\mathbf{u}}^{\mathbf{T}}\boldsymbol{\cdot}\mathbf{H}\boldsymbol{\cdot}\hat{\mathbf{u}}, \tag{91}$$

where $\mathbf{B}$ is the $(M-1) \times M$ first-order, forward finite-difference matrix

$$\mathbf{B} = \begin{pmatrix} -1 & 1 & 0 & 0 & 0 & 0 & 0 & \dots & 0 \\ 0 & -1 & 1 & 0 & 0 & 0 & 0 & \dots & 0 \\ \vdots & & & & \ddots & & & & \vdots \\ 0 & \dots & 0 & 0 & 0 & 0 & -1 & 1 & 0 \\ 0 & \dots & 0 & 0 & 0 & 0 & 0 & -1 & 1 \end{pmatrix}, \tag{92}$$

and $\mathbf{H} = \mathbf{B}^T\boldsymbol{\cdot}\mathbf{B}$ is the $M \times M$ symmetric matrix

$$\mathbf{H} = \begin{pmatrix} 1 & -1 & 0 & 0 & 0 & 0 & 0 & \dots & 0 \\ -1 & 2 & -1 & 0 & 0 & 0 & 0 & \dots & 0 \\ 0 & -1 & 2 & -1 & 0 & 0 & 0 & \dots & 0 \\ \vdots & & & & \ddots & & & & \vdots \\ 0 & \dots & 0 & 0 & 0 & -1 & 2 & -1 & 0 \\ 0 & \dots & 0 & 0 & 0 & 0 & -1 & 2 & -1 \\ 0 & \dots & 0 & 0 & 0 & 0 & 0 & -1 & 1 \end{pmatrix}. \tag{93}$$

Although this choice of constant smoothing leads to a particularly simple form for the matrix $\mathbf{H}$, it is unrealistic to suppose the contaminant concentration profile is almost a constant. Rather, it

would be better to assume that $u(x)$ varies linearly, quadratically or as any some higher polynomial in x. Such different a priori assumptions leads to different $\mathbf{B}$ and $\mathbf{H}$ matrices. Below some more realistic smoothing schemes are proposed.

Linear Smoothing   If we believe a linear function is a good approximation for $C(x) \equiv u(x)$ then with forward finite differences we should minimize

$$\mathcal{B}[\mathbf{u}] \propto \int_0^\infty [\hat{u}''(x)]^2 \, dx \propto \sum_{j=1}^{M-2} [-\hat{u}_j + 2\hat{u}_{j+1} - \hat{u}_{j+2}]^2 \tag{94}$$

so that

$$\mathbf{B} = \begin{pmatrix} -1 & 2 & -1 & 0 & 0 & 0 & 0 & \ldots & 0 \\ 0 & -1 & 2 & -1 & 0 & 0 & 0 & \ldots & 0 \\ \vdots & & & & \ddots & & & & \vdots \\ 0 & \ldots & 0 & 0 & 0 & -1 & 2 & -1 & 0 \\ 0 & \ldots & 0 & 0 & 0 & 0 & -1 & 2 & -1 \end{pmatrix}, \tag{95}$$

which yields for $\mathbf{H} = \mathbf{B}^T \boldsymbol{\cdot} \mathbf{B}$ the $M \times M$ symmetric matrix

$$\mathbf{H} = \mathbf{B}^T \boldsymbol{\cdot} \mathbf{B} = \begin{pmatrix} 1 & -2 & -1 & 0 & 0 & 0 & 0 & \ldots & 0 \\ -2 & 5 & -4 & 1 & 0 & 0 & 0 & \ldots & 0 \\ 1 & -4 & 6 & -4 & 1 & 0 & 0 & \ldots & 0 \\ 0 & 1 & -4 & 6 & -4 & 1 & 0 & \ldots & 0 \\ \vdots & & & & \ddots & & & & \vdots \\ 0 & \ldots & 0 & 1 & -4 & 6 & -4 & 1 & 0 \\ 0 & \ldots & 0 & 0 & 1 & -4 & 6 & -4 & 1 \\ 0 & \ldots & 0 & 0 & 0 & 1 & -4 & 5 & -2 \\ 0 & \ldots & 0 & 0 & 0 & 0 & 1 & -2 & 1 \end{pmatrix}. \tag{96}$$

Quadratic Smoothing   If we believe a quadratic function is a good approximation for $u(x)$ then we should minimize (again use forward finite differences)

$$\mathcal{B}[\mathbf{u}] \propto \int_0^\infty [\hat{u}'''(x)]^2 \, dx \propto \sum_{j=1}^{M-3} [-\hat{u}_j + 3\hat{u}_{j+1} - 3\hat{u}_{j+2} + \hat{u}_{j+3}]^2 \tag{97}$$

so that

$$\mathbf{B} = \begin{pmatrix} -1 & 3 & -3 & 1 & 0 & 0 & 0 & \ldots & 0 \\ 0 & -1 & 3 & -3 & 1 & 0 & 0 & \ldots & 0 \\ \vdots & & & & \ddots & & & & \vdots \\ 0 & \ldots & 0 & 0 & -1 & 3 & -3 & 1 & 0 \\ 0 & \ldots & 0 & 0 & 0 & -1 & 3 & -3 & 1 \end{pmatrix}, \tag{98}$$

33

which yields for $\mathbf{H} = \mathbf{B}^T \cdot \mathbf{B}$ the $M \times M$ symmetric matrix

$$\mathbf{H} = \mathbf{B}^T \cdot \mathbf{B} = \begin{pmatrix} 1 & -2 & -1 & 0 & 0 & 0 & 0 & 0 & 0 & \ldots & 0 \\ -2 & 5 & -4 & 1 & 0 & 0 & 0 & 0 & 0 & \ldots & 0 \\ 1 & -4 & 6 & -4 & 1 & 0 & 0 & 0 & 0 & \ldots & 0 \\ 0 & 1 & -4 & 6 & -4 & 1 & 0 & 0 & 0 & \ldots & 0 \\ 0 & 1 & -4 & 6 & -4 & 1 & 0 & 0 & 0 & \ldots & 0 \\ \vdots & & & & \ddots & & & & \vdots & & \\ 0 & \ldots & 0 & -1 & 6 & -15 & 20 & -15 & 6 & -1 & 0 \\ 0 & \ldots & 0 & 0 & -1 & 6 & -15 & 20 & -15 & 6 & -1 \\ 0 & \ldots & 0 & 0 & 0 & -1 & 6 & -15 & 19 & -12 & 3 \\ 0 & \ldots & 0 & 0 & 0 & 0 & -1 & 6 & -12 & 10 & -3 \\ 0 & \ldots & 0 & 0 & 0 & 0 & 0 & -1 & 3 & -3 & 1 \end{pmatrix} . \tag{99}$$

Second-Order Quadratic Smoothing The use of the first-order forward finite difference approximation for $\hat{u}'''(x)$ in Eq. (97) can be made more accurate for the nodes interior to the boundaries by using a second-order central difference approximation, i.e.,

$$u_i''' \propto [-u_{i-2} + 2u_{i-1} - 2u_{i+1} + u_{i+2}]/2, \quad 2 < i < M - 1. \tag{100}$$

With this approximation, and the first-order forward and backward finite difference approximation for $i = 1, 2, M - 1, M$, the $(M \times M)$ $\mathbf{B}$ matrix becomes

$$\mathbf{B} = \begin{pmatrix} -2 & 6 & -6 & 2 & 0 & 0 & 0 & \ldots & 0 \\ 0 & -2 & 6 & -6 & 2 & 0 & 0 & \ldots & 0 \\ -1 & 2 & 0 & -2 & 1 & 0 & 0 & \ldots & 0 \\ 0 & -1 & 2 & 0 & -2 & 1 & 0 & \ldots & 0 \\ \vdots & & & & \ddots & & & \vdots & \\ 0 & \ldots & 0 & -1 & 2 & 0 & -2 & 1 & 0 \\ 0 & \ldots & 0 & 0 & -1 & 2 & 0 & -2 & 1 \\ 0 & \ldots & 0 & 0 & -2 & 6 & -6 & 2 & 0 \\ 0 & \ldots & 0 & 0 & 0 & -2 & 6 & -6 & 2 \end{pmatrix} . \tag{101}$$

The resulting $\mathbf{H} = \mathbf{B}^T \cdot \mathbf{B}$ is the $M \times M$ symmetric matrix

$$\mathbf{H} = \begin{pmatrix} 5 & -14 & 12 & -2 & -1 & 0 & 0 & 0 & 0 & 0 & 0 & \ldots & 0 \\ -14 & 45 & -50 & 20 & 0 & -1 & 0 & 0 & 0 & 0 & 0 & \ldots & 0 \\ 12 & -50 & 77 & -50 & 8 & 4 & -1 & 0 & 0 & 0 & 0 & \ldots & 0 \\ -2 & 20 & -50 & 49 & -16 & -4 & 4 & -1 & 0 & 0 & 0 & \ldots & 0 \\ -1 & 0 & 8 & -16 & 14 & -4 & -4 & 4 & -1 & 0 & 0 & \ldots & 0 \\ 0 & -1 & 4 & -4 & -4 & 10 & -4 & -4 & 4 & -1 & 0 & \ldots & 0 \\ 0 & 0 & -1 & 4 & -4 & -4 & 10 & -4 & -4 & 4 & -1 & \ldots & 0 \\ \vdots & & & & & & \ddots & & & & & & \vdots \\ 0 & \ldots & -1 & 4 & -4 & -4 & 10 & -4 & -4 & 4 & -1 & 0 & 0 \\ 0 & \ldots & 0 & -1 & 4 & -4 & -4 & 10 & -4 & -4 & 4 & -1 & 0 \\ 0 & \ldots & 0 & 0 & -1 & 4 & -4 & -4 & 14 & -16 & 8 & 0 & -1 \\ 0 & \ldots & 0 & 0 & 0 & -1 & 4 & -4 & -16 & 49 & -50 & 20 & -2 \\ 0 & \ldots & 0 & 0 & 0 & 0 & -1 & 4 & 8 & -50 & 77 & -50 & 12 \\ 0 & \ldots & 0 & 0 & 0 & 0 & 0 & -1 & 0 & 20 & -50 & 45 & -14 \\ 0 & \ldots & 0 & 0 & 0 & 0 & 0 & 0 & -1 & -2 & 12 & -14 & 5 \end{pmatrix} . \tag{102}$$

Cubic Smoothing Finally, we present the smoothing matrix for cubic smoothing. If one uses first-order forward finite differences for the fourth derivative, with cubic smoothing one tries to minimize

$$\mathcal{B}[\mathbf{u}] \propto \int_0^\infty [\hat{u}''''(x)]^2\, dx \propto \sum_{j=1}^{M-4} [-\hat{u}_j + 4\hat{u}_{j+1} - 6\hat{u}_{j+2} + 4\hat{u}_{j+3} - \hat{u}_{j+4}]^2 \tag{103}$$

so that

$$\mathbf{B} = \begin{pmatrix} -1 & 4 & -6 & 4 & -1 & 0 & 0 & \dots & 0 \\ 0 & -1 & 4 & -6 & 4 & -1 & 0 & \dots & 0 \\ \vdots & & & & \ddots & & & & \vdots \\ 0 & \dots & 0 & -1 & 4 & -6 & 4 & -1 & 0 \\ 0 & \dots & 0 & 0 & -1 & 4 & -6 & 4 & -1 \end{pmatrix}, \tag{104}$$

which yields for $\mathbf{H} = \mathbf{B}^T {\bullet} \mathbf{B}$ the $M \times M$ symmetric matrix

$$\mathbf{H} = \begin{pmatrix} 1 & -4 & 6 & -4 & 1 & 0 & 0 & 0 & 0 & 0 & 0 & \dots & 0 \\ -4 & 17 & -28 & 22 & -8 & 1 & 0 & 0 & 0 & 0 & 0 & \dots & 0 \\ 6 & -28 & 53 & -52 & 28 & -8 & 1 & 0 & 0 & 0 & 0 & \dots & 0 \\ -4 & 22 & -52 & 69 & -56 & 28 & -8 & 1 & 0 & 0 & 0 & \dots & 0 \\ 1 & -8 & 28 & -56 & 70 & -56 & 28 & -8 & 1 & 0 & 0 & \dots & 0 \\ 0 & 1 & -8 & 28 & -56 & 70 & -56 & 28 & -8 & 1 & 0 & \dots & 0 \\ 0 & 0 & 1 & -8 & 28 & -56 & 70 & -56 & 28 & -8 & 1 & \dots & 0 \\ \vdots & & & & & \ddots & & & & & & & \vdots \\ 0 & \dots & 1 & -8 & 28 & -56 & 70 & -56 & 28 & -8 & 1 & 0 & 0 \\ 0 & \dots & 0 & 1 & -8 & 28 & -56 & 70 & -56 & 28 & -8 & 1 & 0 \\ 0 & \dots & 0 & 0 & 1 & -8 & 28 & -56 & 70 & -56 & 28 & -8 & 1 \\ 0 & \dots & 0 & 0 & 0 & 1 & -8 & 28 & -56 & 69 & -52 & 22 & -4 \\ 0 & \dots & 0 & 0 & 0 & 0 & 1 & -8 & 28 & -52 & 53 & -28 & 6 \\ 0 & \dots & 0 & 0 & 0 & 0 & 0 & 1 & -8 & 22 & -28 & 17 & -4 \\ 0 & \dots & 0 & 0 & 0 & 0 & 0 & 0 & 1 & -4 & 6 & -4 & 1 \end{pmatrix}. \tag{105}$$

4.3.3 Constrained Linear Regularization (CLR) Method

Often there are physical constraints on the unknown concentration profile $u(x) \equiv C(x)$ which should also be incorporated into the inversion process. For example, one may want $u(x) \geq 0$ or $u_L(x) \leq u(x) \leq u_U(x)$ for specified bounding functions u_L and u_U. In the NDP problem, the concentration profile $u(x)$ clearly must be non-negative. The method of *projections onto convex sets* [Biemond et al. 1990; Press et al. 1992] easily imposes such deterministic constraints if an iterative solution of the functional minimization problem is used.

Many iterative schemes can be used to find the $u(x)$ that minimizes the functional $\mathcal{A}[\mathbf{u}] + \lambda \mathcal{B}[\mathbf{u}]$. An unsophisticated approach is to use the method of steepest descent, whereby the minimum of $\mathcal{A}[\mathbf{u}] + \lambda \mathcal{B}[\mathbf{u}]$ is approached by proceeding from some arbitrary starting point in $\mathbf{u}$ space by taking small steps always in the direction opposite the gradient of $\mathcal{A}[\mathbf{u}] + \lambda \mathcal{B}[\mathbf{u}]$, i.e., downhill. Mathematically, the iteration search is

$$\mathbf{u}^{(k+1)} = \mathbf{u}^{(k)} - \epsilon \nabla (\mathcal{A}[\mathbf{u}] + \lambda \mathcal{B}[\mathbf{u}]), \tag{106}$$

where ϵ is a parameter that determines how far to move downhill in each step. For the linear regularization method, based on minimizing the functional $\mathcal{A}[\mathbf{u}] + \lambda \mathcal{B}[\mathbf{u}] = |\mathbf{A} {\bullet} \widehat{\mathbf{u}} - \mathbf{b}|^2 + \lambda \mathbf{u}^T {\bullet} \mathbf{H} {\bullet} \mathbf{u}$

(see Eq. (85)), the minimization iteration scheme becomes

$$
\begin{aligned}
\mathbf{u}^{(k+1)} &= \mathbf{u}^{(k)} - \epsilon\nabla(|\mathbf{A}\bullet\mathbf{u} - \mathbf{b}|^2 + \lambda\mathbf{u}^T\bullet\mathbf{H}\bullet\mathbf{u}) \\
&= \mathbf{u}^{(k)} - 2\epsilon[(\mathbf{A}^T\bullet\mathbf{A} + \lambda\mathbf{H})\bullet\mathbf{u} - \mathbf{A}^T\bullet\mathbf{b}] \\
&= [\mathbf{1} - \epsilon(\mathbf{A}^T\bullet\mathbf{A} + \lambda\mathbf{H})]\bullet\mathbf{u}^{(k)} + \epsilon\mathbf{A}^T\bullet\mathbf{b}, \quad (107)
\end{aligned}
$$

where, to guarantee convergence [Press et al. 1992],

$$
0 < \epsilon < \frac{1}{\max \text{eigenvalue}\,(\mathbf{A}^T\bullet\mathbf{A} + \lambda\mathbf{H})}. \quad (108)
$$

The converged solution $\lim_{k\to\infty}\mathbf{u}^{(k)}$ will be the same as the LR solution obtained from Eq. (88).

To impose a non-negativity constraint on this iterative solution, define $\mathcal{P}$ as the projection operator that sets to zero all negative components of $\mathbf{u}$. Then modify Eq. (107) to

$$
\mathbf{u}^{(k+1)} = \mathcal{P}\{[\mathbf{1} - \epsilon(\mathbf{A}^T\bullet\mathbf{A} + \lambda\mathbf{H})]\bullet\mathbf{u}^{(k)} + \epsilon\mathbf{A}^T\bullet\mathbf{b}\}, \quad (109)
$$

ensuring that, after each iteration, any negative components of $\mathbf{u}$ are set to zero. The converged solution of this equation is the vector with nonnegative components that minimizes $\mathcal{A}[\mathbf{u}] + \lambda\mathcal{B}[\mathbf{u}]$ using the linear regularization method.

### 4.3.4   Examples of Unfolded Concentration Profiles

Step-Discontinuous Profile

In Fig. 24 the α_2 component of the MCA ion spectrum is shown for a sample with $C(x) = 10^{19}$ atom/cm^3 for $0 \le x \le 2$ μm and zero below 2 μm. This spectrum was calculated using Eq. (70) and the interval average technique of Section 3.6.1. A 256 channel spectrum covering the ion energy range of 0 to 2 MeV was used, and the simulated counts in at least $N = 100$ channels containing the α_2 component were used to unfold the concentration profile at $M = 30$ depths between 0 and 5 μm. This is an example of an over-determined unfolding problem. Further a concentration profile with a step discontinuity is a severe test of any inversion method.

The unfolded profile obtained with the SVD least squares method of Section 4.2.1 is shown in Fig. 25. In this example the simulated counts in channels 90 to 190 ($N = 101$) were used. For this and other NDP unfolding problems, the normal equations for the least squares method are very nearly singular, and the SVD solutions of the normal equations overcomes this near degeneracy nicely (compared to a Gauss elimination solution which gives meaningless results). However, even the SVD least squares profile, while finding the sharp cutoff at $x = 2$ μm, is seen to exhibit small spurious oscillations about the exact profile.
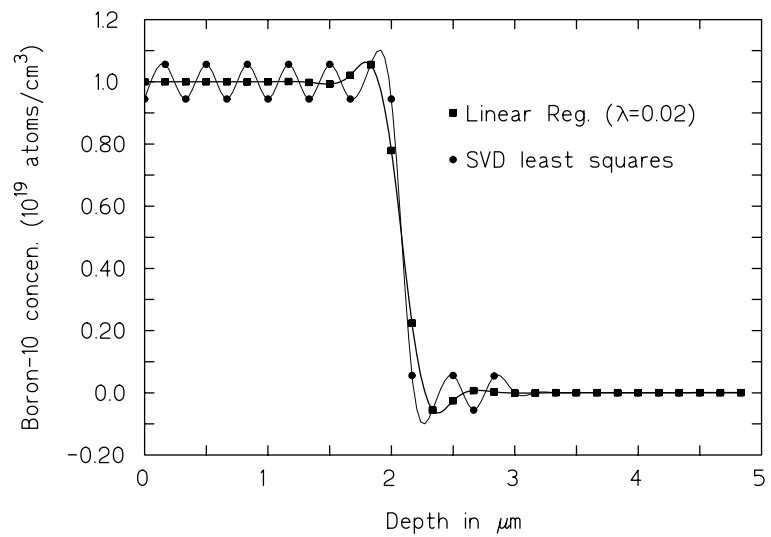
The linear regularization (LR) method is designed for under-determined systems; however, it can also be applied to this over-determined problem. In the LR results shown in Fig. 25, the simulated counts in channels 50–190 ($N = 141$) were used. From these results, the LR estimated profile has no spurious oscillations unlike the SVD-least-squares profile. However, at the dropoff at $x = 2$ μm the LR profile exhibits spurious over and under shoots near the discontinuity. This is largely due to the linear smoothing with the H-matrix of Eq. (96) that was used in the calculations. When constant smoothing is assumed these over and under shoots disappear.

The NIST SRM-2137 Sample

Based on the certified and tabulated ^{10}B concentration in the NIST SRM-2137 sample, the expected 256-channel MCA spectrum for the α_2 ion was estimated over an energy range of 0 to 2 MeV. This
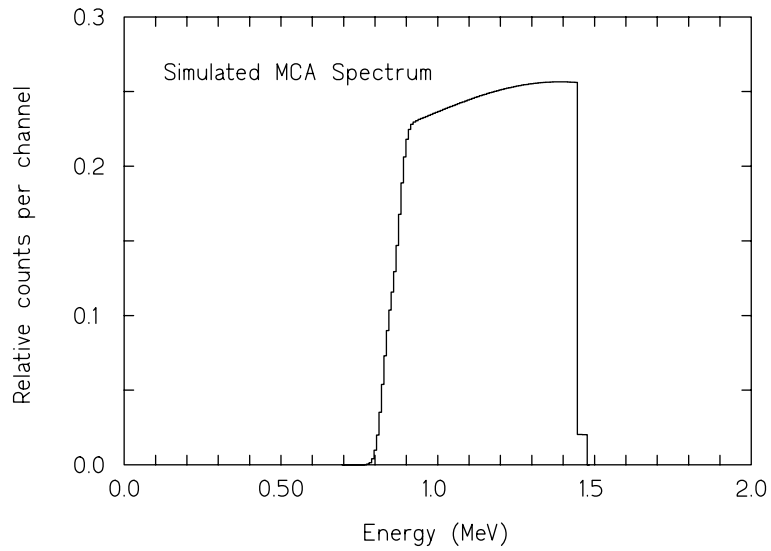
Figure 24. The simulated MCA spectrum for the α_2 ion generated in a sample containing $C(x) = 10^{19}$ ^{10}B atoms/cm^3 for the first two micrometers and no ^{10}B for deeper depths.

Figure 25. The unfolded sample concentration for the simulated spectrum data of Fig. 24. Results are shown for the SVD least squares method (circles) and for the linear regularization method (squares).

MCA spectrum was calculated using Eq. (70) and the interval average technique of Section 3.6.1. Because the ^{10}B in SRM-2137 is distributed only within the first few tenths of μm, most MCA channels had zero counts. Only channels 175–190 (corresponding to midpoint energies of 1.363–1.480 MeV) had non-zero counts. The estimated MCA spectrum is shown in the insert of Fig. 26.

The simulated data in channels 170–190 ($N = 21$) were then analyzed by the LR method to estimate the concentration profile at $M = 30$ sample depths between 0 and 0.5 μm. The solution to this under-determined inverse problem is shown in Fig. 26 along with the certified profile. The inclusion of the simulated data in channels 50–169 (all with zero counts) in addition to that in channels 170–190 produced a highly over-determined problem ($M = 141$) but the LR method produced virtually the same results.

In using the LR inversion technique, a value must be chosen for the parameter λ, which balances the trade off between agreement with the data (the χ^2 term) and the smoothness constraint (the H-term) that regularizes the problem. In the results shown in Fig. 26, the value of λ given by Eq. (89), namely $\lambda = 0.020$ was used. In these results, linear smoothing was used with the H-matrix given by Eq. (96). However, for $10^{-16} \lesssim \lambda \lesssim 10^{-3}$ almost the same results were obtained.

In Fig. 27 the variation of the χ^2 and H terms at the minimum of Eq. (85) is shown as λ varies. The smaller χ^2 the better is the agreement with the data while the smaller H the smoother is the solution. For very large values of λ very smooth profiles are obtained at the expense of poor agreement with the data. By contrast, for very small values of λ, the profile agrees well with the data while the linear smoothness of the profile is compromised. However, if λ becomes too small (here $\lambda \lesssim 10^{-16}$), The H-term contribution in Eq. (85) is lost in the round off of the computer calculations and it ceases to regularize the under-determined set of equations and produces numerically unstable solutions. These effects of extreme values of λ are shown in Figs. 28 and 29.

The large range of values that λ can assume and still give accurate estimates of the concentration profile is deceptive. These examples are for "perfect" data, i.e., data without any stochastic noise. The presence of noise in the data can generally be expected to reduce severely the λ range over which accurate results are produced. However, quantification of this effect is left for future work. Suffice it to say, that the LR method for inverting MCA NDP data to estimate the profile appears to be robust both for the under determined problem (few MCA channels used) as well as for the over determined problem (many MCA channels used).

5 Conclusions

Methods for simulating NDP ion-energy spectra for the case of plane samples and detectors, with arbitrary orientation, have been presented. In particular, several phenomena which broaden or smear the NDP spectra have been modeled, namely (1) energy straggling, (2) detector noise and stochastic energy deposition, and (3) geometric energy broadening. Empirical methods for simulating the first two of these effects have been presented, and a method, based on the emission-angle distribution has been shown to be an efficient method for simulating the latter effect.

With these simulation techniques for estimating NDP spectra, several test spectra have been calculated and used as a basis for testing the robustness of spectral unfolding or inversion techniques. Typically, NDP spectral inversions are over-determined problems if many MCA channels are used. For concentration profiles that are smoothly varying functions of depth, the linear regularization (LR) method is shown to work well for both over-determined and under-determines inversions. Also investigated, for the over-determined unfolding problem, was the method of least squares which is seen to produced spurious oscillations in the unfolded concentration profiles.
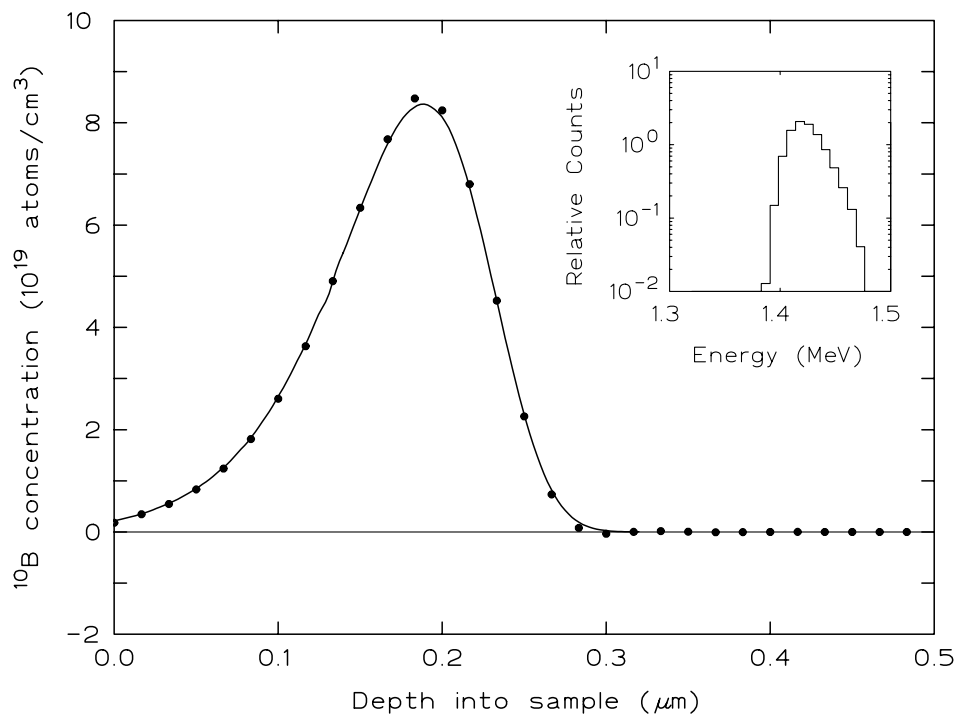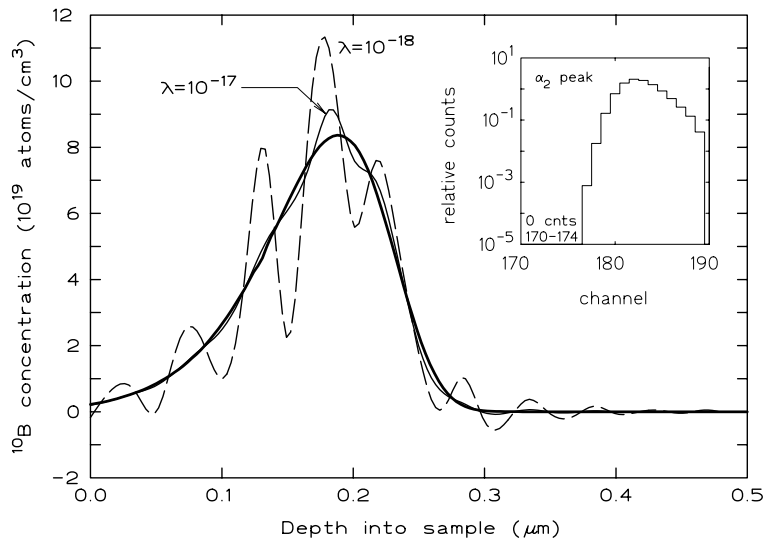
Figure 26. The unfolded concentration profile (circles) using linear regularization compared to the certified profile (line) for the NIST SRM-2137. The simulated NDP spectrum of the α_2 component for this sample is shown in the insert and was used to obtain the unfolded concentration profile.
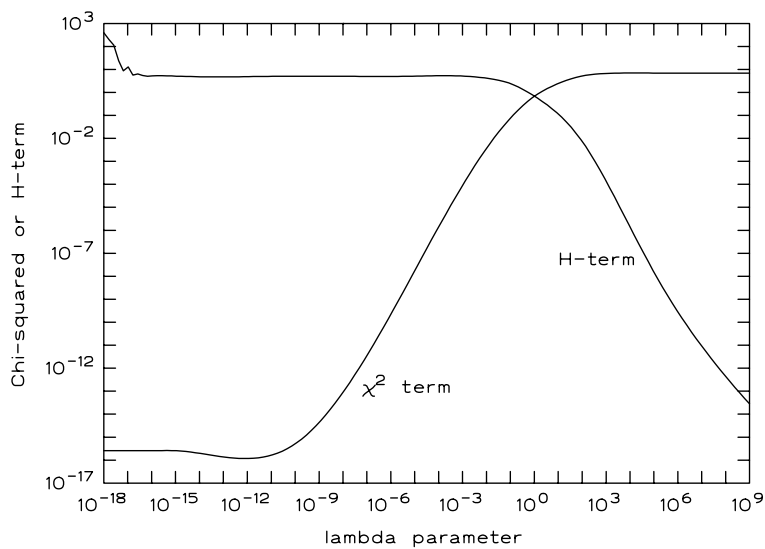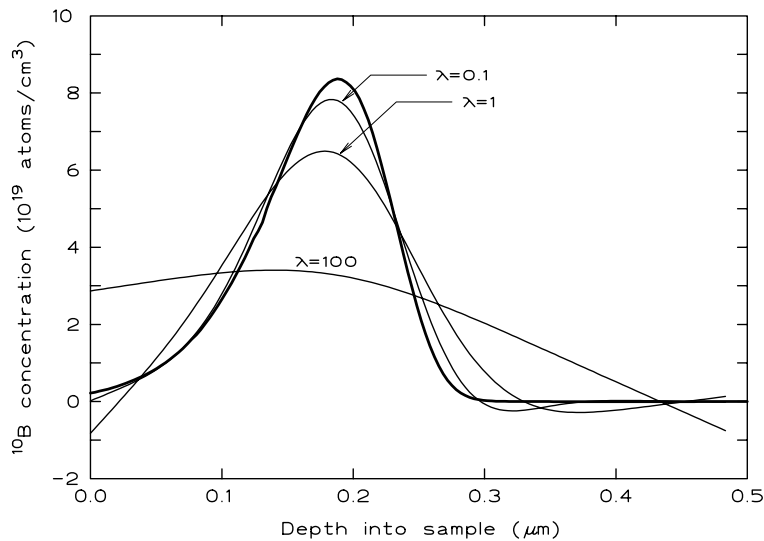

Figure 27. The variation of χ^2 and H-term as λ is varied.

Figure 28. The unfolded NIST SRM-2137 depth profile at $M = 30$ depths using the $N = 21$ counts in channels 170–190 of the simulated MCA spectrum (insert) using the linear regularization method. The heavy line is obtained for $10^{-15} \lesssim \lambda \lesssim 10^{-3}$ and is indistinguishable from the actual certified profile. However, for very small values of λ numerical instabilities are manifested as the regularizing H-term is lost in numerical roundoff errors.

Figure 29. The unfolded NIST SRM-2137 depth profile at $M = 30$ depths using the $N = 21$ counts in channels 170–190 of the simulated MCA spectrum (insert in figure above) using the linear regularization method. The heavy line is obtained for $10^{-15} \lesssim \lambda \lesssim 10^{-3}$ and is indistinguishable from the actual certified profile. However, for very large values of λ the linear smoothing H-term dominates the minimization algorithm and the unfolded profile flattens.

40

BIBLIOGRAPHY

Biemond, J., R.L. Lagendijk, and R. M. Mersereau, *Proceedings of the IEEE*, **78**, 856–883 (1990).

Cittert, P.H. Van, *Z. Phy.*, **69**, 298, 1931.

Cloakley, K.J., R.G. Downey, G.P. Lamaze, H.C. Hoffäss, J. Biegel, and C. Ronning, "Modeling Detector Response for Neutron Depth Profiling," *Nucl. Instr. and Meth. in Phys. Res.*, **366**, 137–144, 1995.

Craig, I.J., and J.C. Brown, *Inverse Problems in Astronomy*, Adam Hilger, Bristol, U.K. (1986).

Hoffman, S., *Practical Surface Analysis by Auger and X-ray Photoelectron Spectroscopy*, Ch. 4, D. Briggs and M.P. Seah (eds.), Wiley, New York, 1983.

Jandel Scientific, "TableCurve," San Mataso, CA, 1996.

Maki, J.T., R.P. Fleming, and D.H. Vincent, "Deconvolution of Neutron Depth Profiling Spectra," *Nucl. Instr. and Meth.*, **B17**, 147-155, 1986.

Miller, K., *SIAM Journal on Mathematical Analysis*, **1**, 52–74 (1970).

Phillips, D.L., *Journal of the Association for Computing Machinery*, **9**, 84–97 (1962).

Press, W.H., S.A. Teukolsky, W.T. Vetterling, and B.P. Flannery, *Numerical Recipes*, 2nd ed., Cambridge Univ. Press, Cambridge, 1992.

Tikhonov, A. N., "The Approximate Solution of Fredholm Integral Equations of the First Kind," *Zh. Vych. Mat.*, **4**, 564–571 (1964).

Tikhonov, A. N., and V. Y. Arsenin, *Solutions of Ill-Posed Problems*, Wiley, New York (1977).

Twomey, S., *Journal of the Association for Computing Machinery*, **10**, 97–101 (1963).

Twomey, S., *Introduction to the Mathematics of Inversion in Remote Sensing and Indirect Measurements*, Elsevier, Amsterdam (1977).

Wertheim, G.K., *J. Electron Spectros. Relat. Phenom.*, **6**, 293, 1975.

Ziegler, J.F. and J.P. Biersack, SRIM-2000.40, "Stopping and Range of Ions in Matter," 2002; available at `http://www.srim.org`